

Contents

1	Introduction	11
1.1	Unsolved questions in black hole astrophysics	12
1.2	Cranking up the angular resolution	17
1.3	The Event Horizon Telescope	18
1.4	A realistic mm-VLBI simulator	22
1.5	Outline	25
2	Theory	27
2.1	Radio Interferometry	27
2.1.1	Measurement Equation	28
2.1.2	Self-calibration and fringe-fitting	31
2.1.3	mm-VLBI observables and data products	33
2.1.4	Variability and the static source assumption	34
2.2	Signal Corruptions	37
2.2.1	Scattering basics	37
2.2.2	Interstellar medium scattering	41
2.2.3	Troposphere	48
2.2.4	Instrumental	58
3	Software implementation	62
3.1	Design objectives	62
3.2	Architechture and Workflow	63

3.2.1	ISM scattering	69
3.2.2	Atmospheric corruption simulator	70
3.2.3	Antenna pointing error simulator	72
4	Results and analysis	73
4.1	Canonical simulations	73
4.2	Suggested applications and improvements	84
5	Conclusion	89
	Bibliography	108

List of Figures

- | | |
|---|----|
| 1.1 (Image credit : Shep Doeleman) Cartoon image (left) combined with the ray-tracing of a thin accretion disc surrounding a BH, first calculated by Luminet [1979]. The cartoon image shows that both the bottom and top of the far side of the accretion disc is lensed by the black hole and is superimposed on the image of the near side of the accretion disc. The dark area in the centre, known as the black hole shadow is the lensed image of the photon ring orbiting the BH. A measurement of its precise shape is a test of general relativity in the strong field regime. Note that the left-right asymmetry in the image is due to doppler boosting. | 16 |
| 1.2 (Image credit: Olaf Frohn ¹) An illustration of angular resolution vs. observing frequency across the entire observational spectrum, shown for a selection of observatories. The VLBI arrays : Spektr-R SVLBI (or RadioAstron) and the EHT clearly achieve the highest angular resolution of all due to their long baselines. At the bottom of the plot, there is a panel showing atmospheric/ionospheric absorption as a function of wavelength, and consequently all observatories in the zero transmission zones are space-based. | 19 |

¹<http://armchairastronautics.blogspot.co.za/p/space-observatories.html>

2.3 Recorded zenith absorption spectrum in the 160 – 520 GHz range, taken on Mauna Kea at an altitude of ≈ 4000 m. The data has been fit to a sum of H ₂ O lines, an H ₂ O pseudo-continuum and dry absorption lines. The model has been generated using the ATM code (see section 2.2.3), with the bottom panel showing the residuals. Here ‘dry’ refers to all atmospheric constituents except H ₂ O. Reproduced from Pardo et al. [2001]	50
2.4 A log-log plot of RMS visibility phase versus baseline length for an observation of 1 Jy source 0748 + 240 with VLA at 22 GHz over a 90 min duration. The open circles show RMS phase as measured whereas the solid squares show the same values with a constant thermal noise contribution of 10° subtracted in quadrature. Note that the measured and theoretical Kolmogorov turbulent exponent β changes with distance on the phase screen as the viewing configuration transitions from a thick screen ($\beta_{\text{theory}} = 5/3$) to a thin screen ($\beta_{\text{theory}} = 2/3$) at $r \approx 1$ km and from a thin screen to completely uncorrelated regime ($\beta = 0$) beyond the outer scale at $r \approx 6$ km. Although these regimes appear distinct, there is continuous variation between them. Reproduced from Carilli and Holdaway [1997]	56
3.1 Flow diagram showing basic sequence of a MEQSILHOUETTE simulation pipeline. The specific sequence is determined by the driver script whereas the logic of each step is contained in an object-oriented framework. The details of the station information, observation strategy, tropospheric and ISM conditions are specified in a user-defined input configuration file. The pipeline is extendable, allowing any additional, arbitrary Jones matrices to be incorporated.	67

3.2	The basic class and module structure of the MEQSILHOUETTE implementation. Solid lines represent a class while dashed lines represent a module. The <i>SimCoordinator</i> class is initialised in the driver script.	68
4.1	“An example simulation of ISM scattering towards Sgr A*, observed with SMT-JCMT-CARMA. The top panel, left to right, shows the original FWHM = 40 μ -arcsec Gaussian (top left), the simulated ISM scattered image on the first night (top middle) and last night (top right) of the observation, respectively. The bottom panel, left to right, shows the evolution of the 10 minute-averaged closure phase with epoch (bottom left), uv-tracks for each night (bottom middle) and the RMS fractional visibility amplitude differences $\sigma_{\Delta V/V_{ea}}$ as a function of <i>uv</i> -distance (bottom right). $\Delta V = (V_a - V_{ea})$, where $ V_a $ and $ V_{ea} $ are the simulated average and ensemble average visibility amplitudes respectively. Variations from the ensemble-average flux on the shortest baselines reveal total flux modulation while flux variations on longer baselines and non-zero closure phases track the fluctuations in sub-structure.” (Image and caption reproduced from Blecher et al. [2016])	76
4.2	“Simulated mean opacity (black) and sky brightness temperature (red) at $\nu = 230$ GHz for three typical ground pressures and temperatures over a typical PWV range [Lane, 1998] which approximately represent the sites of SPT (dots), ALMA (squares) and SMA (triangles). The legend shows the estimated input ground (pressure, temperature) parameters for each site.” (Image and caption reproduced from Blecher et al. [2016])	77

- 4.3 “Simulation of the total delay (left) and the turbulent atmospheric delay (right) for SMA (blue) and ALMA (green) sites towards Sgr A*. Ground pressures and temperatures are the same as Fig. 4.2, precipitable water vapour above each station is set to $w = 2$ mm, and the instantaneous zenith coherence time is set $T_0 = 10$ s for both stations. Note that all tropospheric parameters are, however, independently set. The conversion from time delay to phase at 230 GHz is $1 \text{ rad} = 0.7 \text{ ps}.”$ (Image and caption reproduced from Blecher et al. [2016]) 78
- 4.4 “The effect of residual troposphere phase noise on interferometric images of a point source observed for 12 hours at 230 GHz with 4 GHz bandwidth with the following array : SPT, ALMA, SMA, SMT, LMT and JCMT, assuming the same SEFDs as Lu et al. [2014] and an elevation limit of 15° . For simplicity the weather parameters at each station were set to: coherence time $t_0 = 10$ sec; PWV depth $w = 1$ mm; ground pressure $P = 600$ mb; ground temperature $T = 273$ K. **Top left:** interferometric map with thermal noise only. **Top right:** atmospheric attenuation and sky noise (due to non-zero opacity) with 1% of the turbulent phase noise added. **Bottom left:** as previous but with 3% of turbulent phase contribution. **Bottom right:** as previous but with 6% turbulent phase contribution. The fractional turbulent phase contributions are illustrative of the effect of fringe-fitting errors. The black crosshairs indicate the original source position. ” (Image and caption reproduced from Blecher et al. [2016]) 80

- 4.5 “RMS relative amplitude error induced by pointing error with the 50 m (i.e. fully illuminated) LMT antenna as a function of pointing error offset ρ at 230 GHz. We assume that these errors are degenerate or non-separable from the self-calibration/fringe-fitting model used. See text for the description of the three models used. This simulation capability enables constraints on the magnitude of pointing-induced errors given a particular pointing calibration strategy.” (Image and caption reproduced from Blecher et al. [2016]) 84

List of Tables

2.1 A re-analysis of VLBI observations of Sgr A [*] by Psaltis et al. [2015] has yielded revised estimates of the parameters associated with the Gaussian scattering kernel. Note that the position angle is measured East of North.	43
2.2 Top panel : Closure phases recorded in a VLBA + LMT observation of Sgr A [*] at $\lambda = 3.5$ mm [Ortiz-León et al., 2016]. The data points are shown as red circles and blue squares and are only distinguished by the calibrator used. The green envelopes show the 1σ closure phase prediction induced by scattering-induced substructure. The prediction was generated by simulating interferometric observations of 500 independent realisations of a scattered circular Gaussian with FWHM = 130 μ -arcsec. Reproduced from Ortiz-León et al. [2016]. Bottom panel : Reproduction of the above result using the MEQSILHOUETTE simulator using 50 independent realisations of the scattering screen. The success of the reproduction confirms the functionality of a large section of the simulator.	47

3.1	Top section: keywords of the input configuration dictionary used in a standard simulation similar to that depicted in Fig. 3.1 but without antenna pointing errors. The variable names have been expanded for clarity and keywords which have boolean values have written as questions. In practice, most of these keywords are preceded by an index, which allows this dictionary to be filter into several subdictionaries which can be easily passed to functions or classes. Bottom section: the headings of station weather table whose path is indicated in the input dictionary.	66
3.2	The list of the parameters, aside from the source model, needed to initialise and run SCATTERBRANE. Time variability is made possible as N_{pix} can be a 2-tuple (i.e. a rectangular screen can be created).	69

Chapter 1

Introduction

Black Holes (BHs) are both extreme and ubiquitous objects which are increasingly becoming seen as central to our understanding of the physical universe. The first inferences of their existence came from the observations of the highly energetic Active Galactic Nucleus (AGN) Cygnus A as well as the rapid variability of quasars, both implying a massive and compact engine [e.g. Narayan and McClintock, 2013, and references therein]. Since then, the case for accretion onto a BH powering highly energetic events such as kiloparsec-scale jets and gamma ray bursts have strengthened considerably, however the mechanisms by which these observables are produced are still up for debate. There are also unconstrained questions regarding the nature of the event horizon and the surrounding space-time. The problem in these investigations is that there have been no direct observations which have resolved the innermost black hole emission on event horizon scales. However, this could change within the next few years as new generation of observatory comes into full operation.

1.1 Unsolved questions in black hole astrophysics

We will now provide the astrophysical motivation for this thesis through a discussion of several key questions in black hole astrophysics which could be constrained through observations which resolve the innermost emission region. Later in this chapter we present an upcoming network of telescopes which attempts to achieve this goal.

BHs are formed through the gravitational collapse of a stellar core during a supernovae explosion or from direct collapse from a primordial gas cloud and can grow in mass through accretion of nearby material and/or mergers with other black holes. The observed BH mass distribution is separated into two distinct mass classes, stellar and supermassive - the former with mass on the order $M \sim 10M_{\odot}$ and the latter $M \sim 10^6 - 10^{10}M_{\odot}$ [Falcke and Markoff, 2013]. SMBHs form and reside (unless ejected) in the centres of all galaxies [Kormendy and Richstone, 1995]. Observations of their surrounding galactic bulges show tight correlations between BH mass and both the bulge luminosity and stellar velocity dispersion [Magorrian et al., 1998, Gebhardt et al., 2000], suggesting coevolution or feedback processes.

To constrain the physics near a black hole, the observation needs to be sensitive to scales comparable to the event horizon. For a non-spinning (Schwarschild) black hole, the event horizon is spherically symmetric with a radius,

$$R_{\text{Sch}} = 2R_G = 2GM_{\text{BH}}/c^2, \quad (1.1)$$

where R_G is the Gravitational radius, M_{BH} is the black hole mass, G is the gravitational constant and c is the speed of light. The angular size of such

an event horizon in the far-field approximation is

$$\theta_{\text{Sch}} = R_{\text{Sch}}/d_{\text{src}} \quad (1.2)$$

$$\approx 0.02'' \times 10^{-9} (M_{\text{BH}}/M_{\odot}) (\text{kpc}/d_{\text{src}}), \quad (1.3)$$

where d_{src} is the distance from observer to source.

Due it's size and proximity, the BH with the largest θ_{Sch} turns out to be the SMBH in the centre of our own galaxy, Sgr A*. For Sgr A*, optical/infrared monitoring of orbiting stars [Gillessen et al., 2009] has yielded $M_{\text{BH}} = 4.30 \pm 0.36 \times 10^6 M_{\odot}$ and $d_{\text{src}} = 8.28 \pm 0.32$ kpc. Hence, for Sgr A*,

$$\theta_{\text{Sch}} \approx 10'' \times 10^{-6}.$$

Innermost accretion and jet launch physics

The accretion of gas onto compact objects is a fundamental process in astrophysics, occurring over many orders of magnitude of mass and accretion rate. Closely associated with accretion onto compact objects is the launch of highly energetic, relativistic jets which can remain collimated over huge cosmological distances e.g. Cygnus A. In general, both accretion disks and jets are highly luminous sources, where the dominant emission mechanism is synchrotron radiation which is radiated by relativistic electrons spiralling in a magnetic field. Key features of synchrotron emission is a broad power-law spectrum and strong linear polarisation. Self-absorption accompanies the emission and changes the shape of the spectral energy distribution as the optical depth of such a source is typically inversely proportional to the frequency. The spectral energy distribution of Sgr A* peaks sharply in sub-millimetre, which for a self-absorbed synchrotron source implies that the emission becomes optically thin at these frequencies, and that the sub-millimetre emission arises from event horizon scales. [Serabyn et al., 1997, Falcke et al., 1998].

Theoretical studies and General Relativistic Magneto-Hydrodynamic (GRMHD)

simulations of accreting SMBHs [e.g. Gammie et al., 2003] have provided powerful demonstrations and arguments for how energy and angular momentum is transported in the system, including jet launch mechanisms. Penrose [1969] showed analytically that the rotational energy of a BH could provide the necessary power for jet formation. Associated GRMHD simulations (known as ‘generalised Penrose processes’) typically start with a SMBH surrounded by a torus of gas threaded with a weak (compared to thermal energy) toroidal magnetic field. However, weakly magnetised disks are dynamically unstable if the angular momentum decreases with radius [Balbus and Hawley, 1998]. This differential rotation provides the source of energy in the system as it forms the non-linear Magneto-Rotational Instability (MRI) which in turn creates turbulence in the geometrically thick disc. This turbulence allows the gas to lose angular momentum and gravitational energy, causing mass and magnetic field to be accreted nearer to the BH, in turn causing the inner region of the accretion flow to become highly magnetised. As the BH rotates, magnetic field lines get twisted up by the rotation of the space-time around BH, forming a strong poloidal magnetic field. These “helical magnetic springs” [Narayan et al., 2014] expand, carrying with them, the threaded plasma along the poloidal field lines, launching the jet.

Radiatively Inefficient Accretion Flow [(RIAF), Narayan and Yi, 1995, Yuan et al., 2003] models offer a popular explanation for the $\sim 10^{-8}L_{\text{edd}}$ of Sgr A*. In the RIAF model the electron and proton temperatures decouple due to the low density of the gas. Most of the gravitational energy is converted into the viscous thermal energy of protons which radiate inefficiently compared to electrons. The protons are then either advected into the SMBH or ejected via outflows possibly in the form of winds or a low powered jet. Currently we are still to determine whether the innermost emission of Sgr A* is disc or jet dominated.

In contrast, the powerful jet in M87 is thought to be powered by an accretion disc in the Magnetically Arrested Disc [(MAD), Narayan et al.,

2003] state, wherein mass accretion on the BH is suppressed by the strong magnetic field build-up near the black hole. Compared to Sgr A*, M87 is on the other end of mass and accretion rate spectrum. The location of the jet base in M87 is in relation to its event horizon could help to constrain whether jet powered by the BH as opposed to the accretion disc.

Hence theoretical and computational approaches are beginning to understand these processes, however the range of physical scales needed to be simulated as well as uncertainties in the microphysics make a theoretical approach difficult. Whether or not these process are scale invariant, as suggested by the ‘fundamental plane of black hole activity’ [Merloni et al., 2003], remains to be determined and horizon scale observations are still needed to robustly compare models. Observations which can constrain the configuration of magnetic fields in the inner accretion/jet launch region are essential.

Measuring the black hole shadow

Fortunately, the innermost emission is gravitationally lensed by the SMBH, which causes it to appear magnified by several times its original size. In theory, the innermost orbit should be occupied by a ring of photons, the lensed image of which should feature a shadow-like (or ‘silhouette’) feature [e.g. Johannsen and Psaltis, 2010]. Fig. 1.1 shows a cartoon illustration of the ray tracing combined with an early calculation of the ray-traced image of a thin accretion disc around a BH [Luminet, 1979]. The circular shadow is apparent as the silhouette of the lensed emission originating from the far side of the disc.

Gravity as described by General Relativity (GR) is consistent with all observational experiments thus far [e.g. Kramer et al., 2006], however GR has conceptual weaknesses, especially as it is not compatible with the quantum description of reality. Various alternatives to GR have been theorised which do not assume a purely classical description of matter. To compare GR with the alternatives, we have to compare its predictions in the strong, non-linear

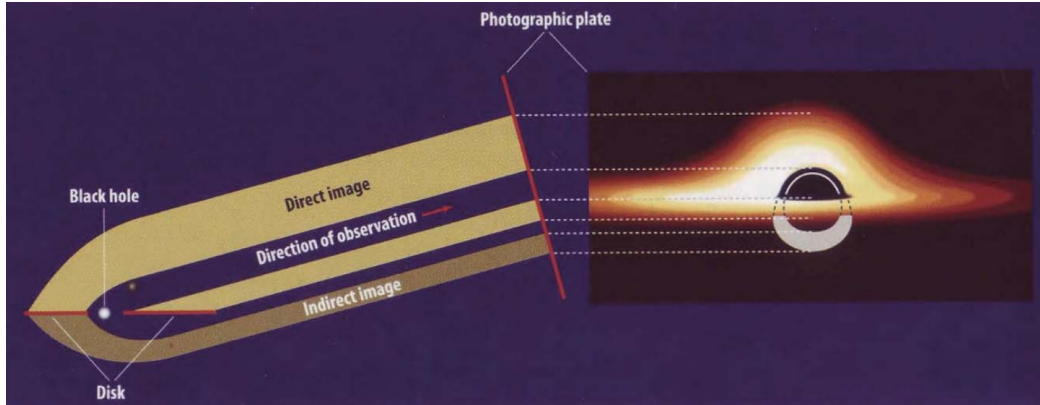


Figure 1.1: (Image credit : Shep Doeleman) Cartoon image (left) combined with the ray-tracing of a thin accretion disc surrounding a BH, first calculated by Luminet [1979]. The cartoon image shows that both the bottom and top of the far side of the accretion disc is lensed by the black hole and is superimposed on the image of the near side of the accretion disc. The dark area in the centre, known as the black hole shadow is the lensed image of the photon ring orbiting the BH. A measurement of its precise shape is a test of general relativity in the strong field regime. Note that the left-right asymmetry in the image is due to doppler boosting.

field regime where the largest deviations from GR would occur if it were an approximate theory.

The space-time within several R_g around a SMBH provides such an opportunity. The precise shape of the photon ring around a SMBH is dependent on the space-time which in turn is calculated within a theory of gravity [Takahashi, 2004]. The No-Hair theorem, which is based on GR, states that the space-time should only be determined by the first two moments of the black hole, i.e. it's mass and spin. If the No-Hair theorem is invalid, the ring will deviate from a Schwarzschild or Kerr profile. In the case of a non-zero quadrupole moment the ring will become either oblate or prolate [Johannsen and Psaltis, 2010].

1.2 Cranking up the angular resolution

Throughout the history of astronomy, there have been celestial sources which appear point-like (unresolved) with the available instrumentation. To investigate the nature of these sources, ever more sophisticated instruments with higher resolution are developed.

In principle, a diffraction-limited aperture can obtain an angular resolution of

$$\theta_{\text{res}} \approx 1.22 \lambda/D, \quad (1.4)$$

where D is the diameter of the aperture and λ is the observing wavelength. However, dish apertures larger than a hundred metres are infeasible to construct while systematic errors, including scattering-induced blurring due to inhomogeneous density (radio) or temperature (optical) distributions in the Earth's atmosphere can lead to instrument being unable to reach the diffraction limit. To overcome these difficulties and improve θ_{res} , a variety of new technologies have been developed (see Fig 1.2), including space-based observatories which escape the limitations set by the Earth's atmosphere, interferometric arrays which eliminate the need to build extremely large apertures, as well as technology-enabled mitigation strategies like adaptive optics and water vapour radiometry which account for atmospheric turbulence in real time.

The observing technique which typically achieves the highest angular resolution is Very Long Baseline Interferometry (VLBI). Interferometry refers to the technique of measuring the electric field correlations (named ‘visibilities’) between pairs of separated antennae. The visibilities are related to Fourier components on a section of approximately flat sky. Through an ‘adequate’ sampling of the Fourier domain an approximate image of sky can be reconstructed using the inverse Fourier transform. With this method, the distance between the antennae (\mathbf{b} , referred to as the ‘baseline’) effectively replaces D in equation 1.4, yielding a higher angular resolution than a single

aperture. This technique is primarily used at radio frequencies while the electric field phase remains relatively stable. VLBI is essentially radio interferometry with antennae separated by large distances, typically $\gtrsim 100$ km, including the possibility for antennae in Earth's orbit. A key distinction from connected-element interferometry is that independent clocks are needed at each station to facilitate the post-observation correlation. VLBI has seen several noteworthy achievements since its inception in the late 1960's, including resolution of the extra-galactic, compact, highly-variable objects, now known as quasars into super-luminal core-jet systems [e.g. Whitney et al., 1971], and the mapping of maser motion around the Super-Massive Black Holes (SMBH) in the cores of nearby galaxies [e.g. Miyoshi et al., 1995].

1.3 The Event Horizon Telescope

Overview

In the last few decades there has been a push to enhance VLBI capabilities at sub-millimetre wavelengths. One of the leading efforts in this regard is the Event Horizon Telescope consortium [(EHT), Doeleman et al., 2010], an international project whose primary objective is to spatially resolve the lensed photon rings of nearby SMBHs with an angular resolution on the order of their event horizons. In contrast to competing high frequency VLBI observatories e.g. the Very Long Baseline Array (VLBA) which has coverage to 87 GHz (3 mm), the EHT is operating at 230 GHz (1.3 mm) and will potentially extend till 345 GHz (0.8 mm) in the future. See Fig. 1.3 for an annotated map of the locations of the EHT array. As the EHT will have baseline lengths comparable to the diameter of the earth, $|b| \sim 10^4$ km and is operating at 1.3 mm, this yields $\theta_{\text{res}} \sim 30 \mu\text{-arcsec}$. The two primary targets Sgr A* and M87 are expected to have gravitationally-lensed photon rings with apparent angular diameters of $\theta_{\text{pr}} \sim 50$ and $\sim 20 - 40 \mu\text{-arcsec}$ respectively [Broderick and Loeb, 2009, Falcke and Markoff, 2013], and hence

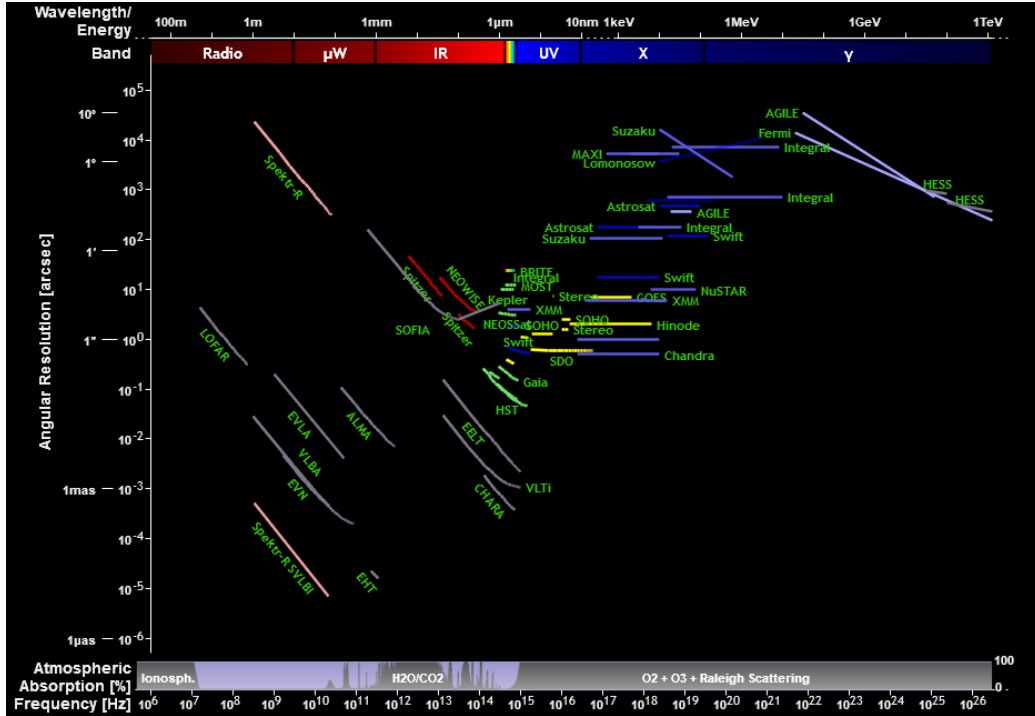


Figure 1.2: (Image credit: Olaf Frohn¹) An illustration of angular resolution vs. observing frequency across the entire observational spectrum, shown for a selection of observatories. The VLBI arrays : Spektr-R SVLBI (or RadioAstron) and the EHT clearly achieve the highest angular resolution of all due to their long baselines. At the bottom of the plot, there is a panel showing atmospheric/ionospheric absorption as a function of wavelength, and consequently all observatories in the zero transmission zones are space-based.

should be resolvable by the EHT.

Instrumentation and observational challenges

The development of mm-VLBI instrumentation has been spurred by the formation of EHT as a project and the deepening of theory and simulation work over the past two decades. This is evidenced by the comparable observational results but starkly different interpretations of Krichbaum et al. [1998] and

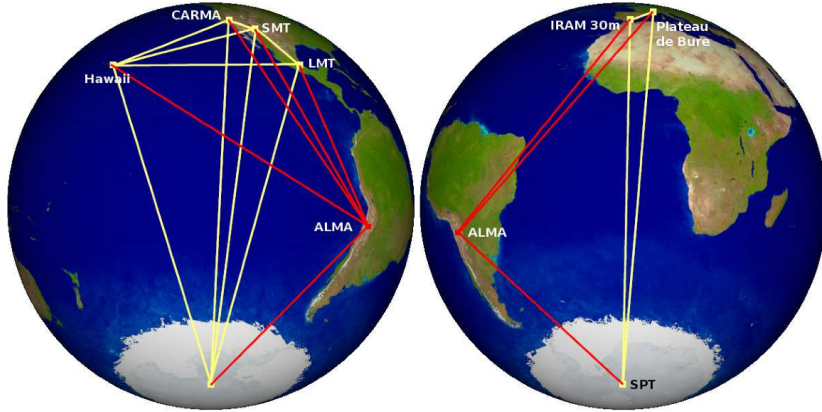


Figure 1.3: (Image credit: Remo Tilanus) The view of the Event Horizon Telescope (EHT) from Sgr A*. This interferometric array uses Earth-diameter baselines, operating at 230–345 GHz to attain an angular resolution of the order of $\theta_{\text{res}} \sim 10 \mu\text{-arcsec}$. Baselines to ALMA are shown in red, to highlight its order of magnitude higher sensitivity. Note that the CARMA station has recently been decommissioned, a telescope in Greenland is currently being constructed and there is ongoing investigation into a possible site on the African continent.

Doeleman et al. [2008]. A decade apart, both teams observed Sgr A* with a mm-VLBI arrays consisting of three stations at similar frequency (215 GHz in 1998 and 230 GHz in 2008). Although the former was limited by calibration uncertainties, the primary difference in analysis and interpretation was that the latter result was linked explicitly to the innermost accretion physics in the event horizon region [e.g. Broderick et al., 2011]. In this way, the newly developed theoretical context contributed to the significance of the Doeleman et al. [2008] result. However, a robust comparison with this diverse body of theoretical work would require a significant leap in mm-VLBI observational capabilities. For example, to discern whether the No-Hair theorem is violated requires the fractional asymmetry of the shadow shape with respect to its angular size to be measured to a few percent [e.g. Goddi et al., 2016, and references therein]. To achieve this level of precision, the development of the

global mm-VLBI array will face significant challenges.

The move to higher frequencies is accompanied by requirements on the instrument including: increased data rates ($1 \rightarrow 16$ GHz) and stability of timing standards; as well as increased accuracy of dish surfaces and antenna pointing accuracy. Difficulties emerge also from the effects of the Earth's lower atmosphere where optical depth becomes significant and turbulence causes rapid fluctuations in the signal transmission time which causes decoherence in the visibilities. Even though the stations are at high altitude, desert locations, the atmospheric coherence times are still short, typically $\lesssim 10$ s [Doeleman et al., 2009]. The extensive requirements on instruments and location drive up the cost of mm-VLBI stations, resulting in few element (< 10) interferometric arrays which make for sparse sampling of the Fourier domain. This is exacerbated by short mutual visibility windows and imperfect weather. Traditional phase referencing calibration is ruled out due to the variable atmosphere, the low sub-mm source density and that calibrators are resolved and variable too at this high angular resolution.

Aside from the considerations listed above, there is a string of complications relating to the sources, the ISM and the calibration procedure. Firstly the emission from the primary source, Sgr A*, is strongly scattered by a turbulent electron plasma in the Interstellar Medium (ISM) along the line-of-sight to the Galactic Centre. This results in a blurring effect [e.g. Fish et al., 2014] which falls as ν^{-2} and become sub-dominant to intrinsic structure in the sub-millimetre range, as shown in Fig. 2.2. This medium both blurs and introduces random, time-variable substructure into the source brightness distribution (see section 2.2.2). The scattering substructure adds complications for data interpretation as its contribution is difficult to disentangle from that of the intrinsic source substructure, depending on the time-scale of the observation. The second issue is that the source is intrinsically variable over minutes to hours (see section 2.1.4). The fact that the source is variable over the course of a single observation epoch breaks a fundamental assumption of the calibration process.

tion in interferometry as the visibilities cannot be related to a static sky image. This (broken) assumption is central to technique of self-calibration and fringe-fitting (see section 2.1.2). These signal corruptions and invalid assumptions appear to interlink in various ways which could generate subtle systematic errors in data analysis.

“These effects, among others, may place significant limitations on the sensitivity, image fidelity, and dynamic range that can be achieved with mm-VLBI observations. Furthermore, unaccounted for systematic and/or non-Gaussian uncertainties could preclude robust, accurate Bayesian parameter estimation and model selection analyses of accretion flow [e.g. Broderick et al., 2016] and gravitational physics [e.g. Broderick et al., 2014, Psaltis et al., 2016], two of the EHT’s many objectives.”

[Blecher et al., 2016]

This point being made is that the data product used in the Bayesian parameter estimation routine, cannot be assumed to have only known Gaussian errors if the calibration procedure did not propagate the full Posterior Probability Distribution (PDF). Thus emerges the imperative for a quantitative understanding of mm-VLBI’s ability to measure and discern between theoretical predictions in the presence of a myriad of signal corruptions.

1.4 A realistic mm-VLBI simulator

Given the significant observational challenges that the EHT faces, we have undertaken this project to build a mm-VLBI observation and signal corruption simulator. There are many benefits for using such a toolkit and indeed synthetic data simulation is common practice for major scientific experiments. A prominent example is the extensive gravitational wave template matching scheme for The Laser Interferometer Gravitational-Wave Observatory (LIGO) which operates in the presence of tidal loading, passing trains

etc. In essence such a simulator would fill in the final component of the theoretical signal propagation chain, effectively taking astrophysical simulations of the source (e.g. accretion onto a SMBH) as an input and returning realistic synthetic interferometric data. This allows a more effective interplay between theory and observation, quantifying systematic effects and the measurement limits. The remainder of this section will briefly discuss several research questions relevant to an EHT synthetic data simulator and how we approach the software design in order to address these questions.

A key use case for simulated data is the testing of calibration, parameter estimation and imaging algorithms and strategies. As the inputs to the simulator are known exactly, we are better able to explore sources of error which are difficult to disentangle from intrinsic source features when using only real data. A straightforward way to perform such a test is through the creation of a set of ‘standard challenge’ dataset. Such datasets would be available to the entire community to input into their calibration and/or imaging routines. Following this, a detailed comparison between the different strategies in varying regimes (source, ISM, troposphere and instrumental) can be made. Importantly, a systematic investigation of a particular algorithm across many different datasets could provide insight into subtle or previously unknowns sources of error inherent in that routine.

Simulated data can also assist in the optimisation of the experimental configuration. Financial constraints require the prioritisation of hardware upgrades e.g. increasing bandwidth, surface accuracy improvement, deployment of water vapour radiometers or additional receiver bands. Simulated data together with calibration and imaging pipelines can help to quantify the benefit of each improvement based on expected scientific return in units of precision of the scientific parameter of interest (e.g. shadow assymetry) rather than more generic terms (e.g. angular resolution, positional uncertainty) that may not have an associated systematic effect included. This approach can even be extended to assess new candidate stations, especially

as new geographic locations (e.g. in Southern Africa) are receiving increasing attention due to the potential long baselines to ALMA, SPT and European stations.

“Over the past decade, significant effort has been placed on advanced radio interferometric calibration and imaging algorithms for centimetre and metre-wave facilities in response to the large number of new arrays in construction or design phase, including MeerKAT, Australian Square Kilometre Array Pathfinder (ASKAP), Square Kilometre Array (SKA), Low-Frequency Array (LOFAR), and the Hydrogen Epoch of Reionization Array (HERA). A leading software package in this pursuit is MEQTREES² [Noordam and Smirnov, 2010], which was developed to simulate, understand and address the calibration issues to be faced with the greatly enhanced sensitivity, instantaneous bandwidth, and field-of-view of such facilities. MEQTREES is rooted in the Measurement Equation mathematical formalism [Hamaker et al., 1996], which parametrises the signal path into distinct 2×2 complex matrices called Jones matrices. This formalism and applications thereof are laid out in [Smirnov, 2011a,b,c] and are arbitrarily generalized to model any (linear) effect, including undesired signal corruptions that often may have subtle, yet systematic effects. MEQTREES has been applied to correct for direction dependent calibration errors to Karl. G. Jansky Very Large Array (VLA) and Westerbork Synthesis Radio Telescope (WSRT) observations, achieving record-breaking high dynamic range images [Smirnov, 2011c, Makhathini et al, in prep.]. The effectiveness provided by the Measurement Equation formalism in radio interferometric calibration provides a strong motivation to explore its application to the challenging goal of imaging a supermassive black hole

²<https://ska-sa.github.io/meqtrees/>

silhouette with mm-VLBI.

Recently, there has been an increase in the attention given to simulating EHT observations of Sgr A* and M87 [Fish et al., 2014, Lu et al., 2014, Bouman et al., 2015, Lu et al., 2016, Chael et al., 2016]. However, these are primarily focused on image reconstruction and assume either negligible or Gaussian distributed gain errors; perfect antenna pointing accuracy; and in most cases only Gaussian convolution to simulate ISM scattering. Clearly, as the EHT array is enhanced (and possibly expanded), so too must the interferometric simulations evolve to provide ever-more physical predictions on the confidence levels with which parameters can be extracted and hence exclude theoretical models of gravity and/or accretion flows.

Given the significant, yet surmountable, observational challenges that the EHT faces, we have undertaken a project to leverage metre and cm-wavelength simulation and calibration successes and build a MEQTREES-based mm-VLBI-specific software package called MEQSILHOUETTE. While MEQTREES has not yet been used in the context of mm-wavelength observations, the framework is agnostic to higher frequency implementation as long as the Measurement Equation is appropriately constructed. MEQSILHOUETTE enables realistic interferometric simulations of mm-VLBI observations in order to gain deeper understanding of a wide range of signal propagation and calibration effects.”

[Blecher et al., 2016]

1.5 Outline

This thesis is divided into the following chapters and sections,

- **Chapter 2 : Theory**

Section 2.1 introduces radio interferometry via the Measurement Equation formalism, followed by mm-VLBI tailored discussions on calibration, data products and the consequences of breaking the static source assumption.

Section 2.2 is a review and investigation into the key signal corruptions implemented in the MEQSILHOUETTE simulator i.e. instrumentation imperfections and transmission through the ISM and Earth's atmosphere.

- **Chapter 3 : Software Implementation**

Section 3.1 summarises the key software design objectives considered.

Section 3.2 is a description of the design and construction of the simulation software with emphasis on the software architecture and workflow.

- **Chapter 4 : Results**

Section 4.1 showcases the basics of the simulator output through a series of canonical results.

Section 4.2 presents a more sophisticated scenario which tests an AIPS calibration routine in the presence of source and tropospheric time-variability.

- **Chapter 5 : Discussion**

Section 5.1 explores the implications of the results shown in the previous chapter.

Section 5.2 makes suggestions for future applications of and improvements to the simulator.

- **Chapter 6 : Conclusions**

We summarise the work and context of this thesis.

Chapter 2

Theory

In this chapter we review and develop the theory required to model signal transmission from cosmic source to uncalibrated (raw) interferometric data. The first half of this chapter provides the necessary introduction to fundamental radio interferometric concepts while the second half is focused specifically on describing several key signal corruptions, relevant to mm-VLBI observations.

2.1 Radio Interferometry

This section is structured as follows: first radio interferometry is introduced using the Radio Interferometric Measurement Equation (RIME) formalism, which serves as a guiding framework for the construction of the MEQSILHOUETTE simulator. We then review the technique of self-calibration, typical mm-VLBI data products and the consequences of breaking the static source assumption.

2.1.1 Measurement Equation

The RIME provides the notation and formalism to model the signal transmission path as a sequence of linear operations. It takes into account polarisation, correlation and the correct time-ordering of signal transmission path in an intuitive and efficient way. The formalism also enables a more informative phrasing of the relation between calibration and signal corruptions.

Here we offer a short derivation and explanation of the RIME following Smirnov [2011a]. Consider a quasi-monochromatic, complex-valued electric field vector \mathbf{E} , which can be decomposed into an arbitrary two dimensional orthogonal basis in the plane perpendicular to the direction of propagation,

$$\mathbf{E} = \begin{pmatrix} E_a \\ E_b \end{pmatrix},$$

where this choice represents the basis in which the polarisation is measured. All linear transformations of the above electric field can be written by a multiplication with a 2×2 complex valued matrix, termed a *Jones* matrix [Jones, 1941],

$$\mathbf{E}' = \mathbf{J}\mathbf{E}. \quad (2.1)$$

For example, the conversion of the electric field to a voltage \mathbf{v} at an antenna can be specified by such a transformation i.e. $\mathbf{v} \equiv \mathbf{E}'$ under multiplication with the appropriate \mathbf{J} . Multiple effects then can be represented by multiplication of various Jones matrices, forming a Jones chain,

$$\mathbf{E}' = \mathbf{J}_n \dots \mathbf{J}_1 \mathbf{E}. \quad (2.2)$$

The order of the Jones matrices should obey the causal order of the signal transmission path (i.e. \mathbf{J}_1 would occur closest to the source, \mathbf{J}_n closest to the antenna). However, the rules of commutivity of matrices allows us some flexibility. Matrices which are scalar commute with everything, while diagonal matrices commute with each other as do matrices which effect

a rotation of \mathbf{E} . This allows the Jones chain to be re-ordered into more convenient formulations as required. In other words, the signal path can be parameterised in different ways. For example during calibration, it is useful to construct a *phenomenological* Jones matrix which represents the combined action of several *physical* commuting processes/matrices (e.g. ionospheric delay and electronic drift). The advantage would be that only the cumulative effect is considered, which keeps the number of parameters to solve for to a minimum. This would be useful when the individual effects cannot be easily distinguished and/or have the same Jones matrix form. On the other hand, for realistic data simulation, we prefer to model the signal transmission path by formulating a Jones matrix based on the exact physical process.

An interferometer measures the correlation of the voltages from an antenna pair, referred to as a *baseline*. The correlator output is termed the *visibility*,

$$\mathbf{V}_{pq} = \langle \mathbf{v}_p \mathbf{v}_q^H \rangle, \quad (2.3)$$

where p, q refer to the two antennae. The representation of \mathbf{V}_{pq} as a 2×2 matrix is equivalent to the Stokes polarisation formulation, for example in an XY basis,

$$\mathbf{V}_{pq} = \mathbf{J}_p \langle \mathbf{E}_p \mathbf{E}_q^H \rangle \mathbf{J}_q^H \quad (2.4)$$

$$= \mathbf{J}_p \begin{pmatrix} \langle E_{xp} E_{xq}^* \rangle & \langle E_{xp} E_{yq}^* \rangle \\ \langle E_{yp} E_{xq}^* \rangle & \langle E_{yp} E_{yq}^* \rangle \end{pmatrix} \mathbf{J}_q^H \quad (2.5)$$

$$= \mathbf{J}_p \begin{pmatrix} I + Q & U + iV \\ U - iV & I - Q \end{pmatrix} \mathbf{J}_q^H, \quad (2.6)$$

where I is the coherence of the total flux, V is the coherence of the circularly polarised flux, Q and U relate to coherence of the linear polarisation. Note that the Jones matrices are assumed to be constant over the time and frequency averaging interval. As this formalism is coordinate system inde-

pendent, we can easily transform any 2×2 from a linear to circular basis and vice-versa.

We now review the RIME for a single, uncorrupted, unpolarised point source, which will illustrate the Fourier transform relation between the measured visibility and a section of approximately flat sky. Considering that there are no signal corruptions, the only Jones matrix to consider is the effect of the phase difference of the electric fields measured at the two antennae. This is due to the difference in geometric propagation path length.

Consider the unit vector $\hat{\sigma}$ which points from the centre of the Earth towards the source. We define the position difference between the two antenna or baseline vector in a convenient coordinate system as $\mathbf{u} = (u, v, w)$, with the w -axis in the direction of $\hat{\sigma}$. Next we denote the angular position on the sky by (l, m) which are the directional cosines on the sky measured in the direction of (u, v) respectively. Note that we consider only a small approximately flat section of the celestial sphere centred on $\hat{\sigma}$, also called the *phase centre*. The phase difference between rays arriving at the two antennae is therefore,

$$\delta\phi = 2\pi(\mathbf{u}/\lambda \cdot \hat{\sigma}) \quad (2.7)$$

As we are only interested in a small, approximately planar component of the sky (i.e. $l^2 + m^2 \ll 1$),

$$\delta\phi \approx 2\pi\lambda^{-1}(u_p l + v_p m). \quad (2.8)$$

Denoting the brightness matrix $\mathbf{B} = \langle \mathbf{E}_p \mathbf{E}_q^H \rangle = \mathbf{1}$ and setting the delay of antenna q as the reference, the RIME for our simplified model becomes

$$\mathbf{V}_{pq} = K_p \mathbf{B} K_q^H \quad (2.9)$$

$$= [\exp(2\pi i\lambda^{-1}(ul + vm))] \mathbf{B} [1] \quad (2.10)$$

where K_p was the Jones scalar matrix used to apply the relative phase dif-

ference between the two antennae.

Equation. 2.9 expresses a Fourier Transform relation between visibility domain (u, v) (spatial frequency) and the image domain (l, m) . This derivation can be easily broadened to include extended sources (e.g. see [Smirnov, 2011a]). The quantity $K_p \mathbf{B} K_q^H$ is often denoted as \mathbf{X}_{pq} and is termed the coherency matrix.

An example of a Jones matrix expressing a signal corruption is the complex time-variable antenna gain. Considering two independent linear dipoles, for antenna p

$$\mathbf{G}_p(t) = \begin{pmatrix} g_x(t) & 0 \\ 0 & g_y(t) \end{pmatrix} \quad (2.11)$$

Our RIME with antenna gains included becomes,

$$\mathbf{V}_{pq} = \mathbf{G}_p \mathbf{X}_{pq} \mathbf{G}_q^H. \quad (2.12)$$

2.1.2 Self-calibration and fringe-fitting

We now discuss two (similiar) calibration algorithms frequently used in VLBI: self-calibration and fringe-fitting. These algorithms are used to solve for station based gain terms, i.e. \mathbf{G} -Jones terms, knowledge of which is essential to extract information of the actual sky. Later in this chapter, we show how signal corruptions e.g. turbulence in the Earth's troposphere or timing errors can lead to rapid variability in the \mathbf{G} -Jones terms, making them difficult to determine. Our motivation is that we are interested how these algorithms fare in the context of the unique observational challenges faced by the EHT (see section 1.3). Crucially, MEQSILHOUETTE is able to provide the synthetic datasets on which these algorithms can be tested.

Self-calibration, as the name suggests, uses the target itself as a calibrator to estimate station gains. The algorithm consists of the following, simplified iteration:

1. assume an initial sky model (typically a point source if observing a

known bright calibrator),

2. solve for station gains (but not their derivatives) in equation 2.12,
3. image and deconvolve (i.e. the effect of the synthesised beam is partially removed)
4. run source finder and update sky model,
5. repeat steps 2 to 4 until a specified flux threshold is reached.

Fringe-fitting ('fringe' is an alternative term for visibility phase) is similar to self-calibration as it also solves for station gains in equation 2.12 whilst assuming a source model. However fringe-fitting is typically run before self-calibration. Its emphasis is less focused towards building a complete sky model and more towards optimising phase coherence and hence SNR. This is not a problem for connected element interferometry where phases are more coherent and voltages are correlated immediately.

Instead of a solver, fringe fitting is primarily a grid search across the first order derivatives of the station gain phases with respect to time and frequency. These derivatives are often phrased in terms of station time delays \tilde{t}_p (often shortened to 'delay'), where p is the antenna, and the rate of change in time delays $r_p = \partial_t \tilde{t}_p$ (often shortened to 'rate'). Hence \mathbf{G} for antenna p in equation 2.12 is expanded to,

$$\mathbf{G}_p(t, \nu) = \exp [-i(\phi_0 + 2\pi\tilde{t}_p\nu + 2\pi r_p * t)] . \quad (2.13)$$

Note that the solution time interval is specified by the user. The gain amplitude are often calibrated separately, reducing the number of parameters to optimise. The sky model used is typically just a point source at the centre of the field, however more complex sky models may be manually iterated upon and manually assessed.

2.1.3 mm-VLBI observables and data products

If the visibility amplitude and phase are highly variable as in the case of a turbulent atmosphere with non-negligible opacity, conventional calibration and imaging techniques have severely limited (if any) success. However, information can still be extracted from the raw visibilities in the form of closure quantities [Monnier, 2007] or polarisation ratios [?]. Visibility amplitudes are also used although they suffer from systematic errors, a subset of which are dealt with in this work. Closure phase, defined as the sum of visibility phases of a triangle of stations $\{i, j, k\}$, is a probe of point-asymmetry in source structure,

$$\Phi_{ijk} = \phi_{ij} + \phi_{jk} + \phi_{ki}. \quad (2.14)$$

Because many of the dominant signal corruptions are station-based, the gain phase terms $\phi_{ij} = \phi^{\text{true}} + \phi_i^G - \phi_j^G$ for each antenna, assuming they are constant over the integration time and bandwidth, will cancel which yields a more robust observable.

In the literature, the uncertainty on the closure phase is calculated in various ways. One method which is typically used for simulation/prediction is model dependent and is given as a function of the SNR s_{ij} of each baseline [Rogers et al., 1995],

$$u(\Phi_{ijk}) = \frac{\sqrt{4 + (s_{ij}s_{jk})^2 + (s_{jk}s_{ki})^2 + (s_{ij}s_{ki})^2 + 2(s_{ij}^2 + s_{jk}^2 + s_{ki}^2)}}{s_{ij}s_{jk}s_{ki}}, \quad (2.15)$$

where s_{ij} is defined as

$$s_{ij} = |V_{ij}| \sqrt{\frac{\tau \Delta \nu}{SEFD_i SEFD_j}}, \quad (2.16)$$

where τ is the vector averaging timescale, $\Delta\nu$ is the bandwidth, $|V_{ij}|$ is the visibility amplitude of the assumed source model and $SEFD$ is the system

equivalent flux density.

Some imaging algorithms use a technique called ‘hybrid mapping’ [e.g. Skilling and Bryan, 1984, Bouman et al., 2015, Chael et al., 2016] which use closure phase as a regulariser to ensure that imperfect calibration of station gains do not affect the resulting image, although these unconventional imaging algorithms come with their own uncertainties on uniqueness and repeatability.

2.1.4 Variability and the static source assumption

Implicit in our description of interferometry above (see equation 2.9), we assumed that the source remains approximately unchanged or static during the course of the observation. However, if this assumption does not hold (i.e. if the source is time-variable), the visibilities measured over the course of an observation can no longer be related to a single image. Note that I am using the term ‘variability’ in a general sense which refers to changes in any source observables. Variability is most often used to denote changes in source flux but we extend the definition to include changes in source structure, position and polarisation.

Although the static source assumption holds for most interferometric observations, the accretion flow and/or magnetic field structures around a SMBH can be variable on far shorter timescales. The primary mm-VLBI target, Sgr A*, exhibits variability on timescales of minutes to hours in the high frequency radio (including EHT observations), near-infrared (NIR), and X-ray bands [e.g. Baganoff et al., 2001, Genzel et al., 2003, Yusef-Zadeh et al., 2006, Marrone et al., 2006, Fish et al., 2011, Johnson et al., 2015]. This wealth of observational data has yielded several constraints but the origin of the variability is still highly debated.

In principle, the variability timescale could be comparable to the period of the Innermost Stable Circular Orbit (ISCO), which for Sgr A*, ranges from 4 minutes in the case of a maximally rotating BH with a prograde disc

to about half an hour for a non-rotating BH. The ISCO period for M87 is substantially longer, on the order of days. Considering light crossing times Δt_{cross} , we estimate the intrinsic size Δx of the emission region to be of order $\Delta x \sim \Delta t_{\text{cross}} c$, where c is the speed of light. Hence a flare of duration $\Delta t_{\text{cross}} = 10$ min corresponds to scales of $\Delta x < 15R_{\text{Sch}}$. Such analyses of Sgr A* gave early evidence for an emission area on event horizon scales.

Furthermore we considered separating source variability into the following interlinked modes : static flaring regions, changes in magnetic field/polarisation and spatial variability in total intensity. Each of the different modes may inform different approaches to calibration and parameter extraction especially when using different quantities e.g. closure phases vs. polarisation ratios. It might be necessary to split the observation into several sub-intervals which are calibrate separately although the determination of the sub-intervals is an open question. Following this, we outline the role of MEQSILHOUETTE to assist with the analysis and interpretation. It has also been proposed by Lu et al. [2016] that a Gaussian weighting scheme can be applied to mitigate the effects of variability and measure the quiescent structure although this approach would down-weight the longest baselines, losing information of the finer angular scales.

By far the most well studied type of variability, is simply variations in total flux, referred to as flares. To explain the observed delays between flares in different frequency bands, an expanding adiabatic plasma model [e.g. Marrone et al., 2008] has been presented, however a recent flare observed with the EHT did not exhibit the increase in size expected from an expanding plasma outflow model Fish et al. [2011]. This highlights the importance of synchontron self-absorption and the variable size of emission region, as the $\tau \sim 1$ surface is frequency dependent, simultaneous multi-wavelength observations could lead to a more profitable EHT variability analysis.

Secondly, consider a source structure which is varying primarily in spatial position in the innermost flow, e.g. an orbiting unresolved component or jet

launch region e.g. a shock. Signatures of periodic variability at NIR and X-ray [Genzel et al., 2003, Bélanger et al., 2006] have been used to argue for the presence of orbiting hotspots Doeleman et al. [2009]. As the Innermost Stable Circular Orbit (ISCO) depends on spin of the BH, the spin can be constrained through the detection periodic orbital features. In the case of an compact, unresolved variable component, several approaches [Doeleman et al., 2009, Fish et al., 2009, Johnson et al., 2014] show that EHT can track such a structure with $\sim 5 \mu\text{-arcsec}$ precision using closure quantities and polarimetric ratios, assuming that ALMA is participating in the array. On the other hand, a more recent observation of a longer, 600 minute light curve in the NIR is more representative of a power-law scale variability Meyer et al. [2008] which could be explained by power-law turbulence.

Another possible ‘mode’ of variability is one that is primarily based on magnetic field structures. A recent mm-VLBI result is that variability in the polarisation domain is far more rapid than the total intensity [Johnson et al., 2015], indicating that the magnetic field structure is highly dynamic, see section 1.1.

As stated earlier, the standard mm-VLBI calibration techniques i.e. fringe-fitting, assume that the source is static over the course of the observation. However, if this is not the case, these techniques should be tested to check the consequences of using them under this broken assumption. These effects could limit image fidelity and DR, but could also cause systematic effects relevant to the EHT measurement objectives (e.g. shadow asymmetry). To help characterise the errors in this scenario, it is important that MEQSIL-HOUETTE has the capability to handle time variability of the source in a consistent manner with the rest of the simulator.

2.2 Signal Corruptions

In this chapter we explore in detail signal corruptions due to the transmission through the ISM and Earth’s atmosphere as well as instrumental imperfections, in order for these corruptions to be implemented in the MEQSILHOUETTE simulator. Whilst there are many additional potential sources of error (e.g. clock errors, bandpass, polarisation leakage, phasing errors, quantisation, correlator model etc.). The point of this investigation is to demonstrate a mm-VLBI framework that enables more sophisticated interferometric simulations. As such, we have focused on capabilities not present in other mm-VLBI simulations and those which represent different implementation forms (i.e. the troposphere, ISM and antenna pointing errors). These also represent amongst the most challenging signal corruptions to implement and present the biggest calibration and parameter estimation and imaging challenges. The MEQSILHOUETTE framework, rooted in the Measurement Equation formalism, enables any arbitrary error to be incorporated as a Jones Matrix (e.g. correlator model error is a simple scalar matrix). Our intention here is to demonstrate some of the key features of MEQSILHOUETTE and its potential to provide realistic mm-VLBI simulations for systematic studies.

2.2.1 Scattering basics

This subsection (with exception of Fig.2.1 has been reproduced from Blecher et al. [2016]).

Millimetre wavelength radiation originating at the Galactic Centre is repeatedly scattered along the signal path to the Earth-based observer. The first occurrence is due to electron plasma in the ISM [e.g. Bower et al., 2006, Gwinn et al., 2014], while the second is due to poorly-mixed water vapour in the Earth’s troposphere [e.g. Lay, 1997, Carilli and Holdaway, 1999]. It is essential that the effects of the scattering phenomena are understood for accurate calibration and robust inference of the intrinsic source properties.

As an introduction to the separate descriptions of each, we review a simple scattering model.

An electro-magnetic wave is scattered when it passes through a medium with refractive index inhomogeneities. Following Narayan [1992], this effect can be modelled as a thin screen, located between source and observer planes and orientated perpendicular to the line-of-sight. The screen, with 2D coordinates \mathbf{x} , adds a stochastic phase $\phi(\mathbf{x})$ to the incoming wave at each point on the screen, yielding a corrugated, outgoing wavefront. We define the Fresnel scale as $r_F = \sqrt{\lambda D_{os}/2\pi}$, where D_{os} is the observer-scatterer distance. r_F represents the distance where the geometrical path difference $\frac{2\pi}{\lambda}(D_{os} - \sqrt{D_{os}^2 + r_F^2}) = \frac{1}{2}$ rad.

To determine the resultant electric field at a point in the plane of the observer, indexed by coordinate vector \mathbf{X} , one has to take into account all possible ray paths from the screen to \mathbf{X} . To illustrate the model, a calculation of the scalar electric field generated by a point source, $\psi(\mathbf{X})$ yields the Fresnel-Kirchoff integral [Born and Wolf, 1980]

$$\psi(\mathbf{X}) = C \int_{\text{screen}} \exp \left[i\phi(\mathbf{x}) + i\frac{(\mathbf{x} - \mathbf{X})^2}{2r_F} \right] d\mathbf{x}, \quad (2.17)$$

where C is a numerical constant.

The statistical properties of $\phi(\mathbf{x})$ can be described by a power spectrum or equivalently the phase structure function,

$$D_\phi(\mathbf{x}, \mathbf{x}') = \langle [\phi(\mathbf{x} + \mathbf{x}') - \phi(\mathbf{x})]^2 \rangle, \quad (2.18)$$

where \mathbf{x} and \mathbf{x}' represent two points on the screen and $\langle \dots \rangle$ denotes the ensemble average.

There is evidence that D_ϕ can be reasonably approximated by a power law dependence on the absolute distance r between points on the screen

[Armstrong et al., 1995, Carilli and Holdaway, 1997]

$$D_\phi(r) = (r/r_0)^\beta, \quad r^2 = (\mathbf{x} - \mathbf{x}')^2 \quad (2.19)$$

where r_0 is the phase coherence length scale defined such that $D_\phi(r_0) = 1$ rad. Kolmogorov turbulence, which describes how kinetic energy injected at an outer length scale r_{out} cascades to increasingly smaller scales until finally dissipated at an inner length scale r_{in} , predicts $\beta = 5/3$ in the domain $r_{\text{in}} << r << r_{\text{out}}$. This scaling has been demonstrated to be a reasonable approximation for the ISM over scales $r \sim 10^2$ km to > 1 AU [Johnson and Gwinn, 2015], and also for the troposphere with $r < \Delta h$, where Δh is the thickness of the turbulent layer Coulman [1985]. The specifics of the tropospheric model will be explored further in section 2.2.3.

The two length scales, r_F and r_0 , define the nature of the scattering which is split into the strong and weak regimes (see Fig. 2.1). In the weak scattering regime, $r_0 \gg r_F$ and hence by equation 2.19, $D_\phi(r_F) \ll 1$. This implies that most of the radiative power measured on a point \mathbf{X} will originate from a screen area $A_{\text{weak}} \approx \pi r_F^2$. Whereas in the regime of *strong scattering*, $r_0 \ll r_F$ yielding $D_\phi(r_F) \gg 1$. This results in coherent signal propagation onto the point \mathbf{X} from multiple, disconnected zones, each of area $A_{\text{strong}} \approx \pi r_0^2$ [Narayan, 1992]. Scattering in the troposphere and ISM towards the Galactic Centre fall into the regimes of weak and strong scattering respectively.

To evolve the screen in time, we assume a frozen screen model i.e. that the velocity of the individual turbulent eddies is dominated by the bulk motion of scattering medium [e.g. Lay, 1997]. This allows us to treat the screen as frozen but advected over the observer by a uniform motion. Hence, time variability can be easily incorporated by the relative motion between source, scattering screen, and observer.

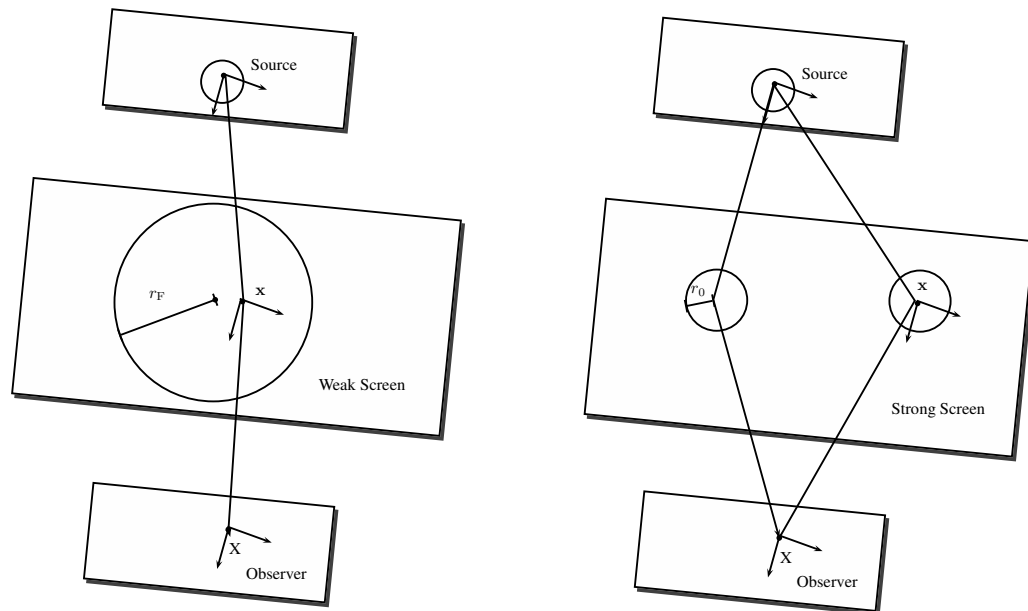


Figure 2.1: Illustration depicting the basics of scattering in the weak (left) and strong (right) regimes. In the weak regime, the signal is coherently propagated over an area, $A_{\text{weak}} \approx \pi r_F^2$, whereas in the strong regime, coherent propagation is split over many areas, each of size $A_{\text{strong}} \approx \pi r_0^2$.

2.2.2 Interstellar medium scattering

Electron density inhomogeneities in the interstellar medium (ISM) plasma scatter the radio waves propagating through it, increasingly so towards the Galactic Centre. Radio interferometric observations of Sgr A* have characterised the basic properties of the intervening plasma material, however extensive developments in scattering theory and simulations have proved essential to the interpretation of more subtle scattering phenomena. This section begins with previous VLBI results which studied the Gaussian blurring effect of the scattering of Sgr A*. We then expand on the scattering theory introduced in Sec. 2.2.1 to review the latest theoretical developments which explore the presence of scattering-induced substructure. Finally, we review recent observational results which account for scattering substructure in their data interpretation.

The dominant observational effect of this scattering scenario for $\lambda \gtrsim 1$ cm is to convolve the intrinsic source structure with an elliptical Gaussian. The size of the Gaussian exhibits a λ^2 scaling dependence over several orders of magnitude [Fig. 2.2 Backer, 1978, Shen et al., 2005, Bower et al., 2006, Lu et al., 2011], which is consistent with the wavelength dependence of the refractive index of a plasma. In order to determine the parameters of the scattering kernel, i.e. major axis, minor axis and position angle, one has to observe at wavelengths where the angular size of scattering ellipse is much larger than the expected source size. A Very Long Baseline Array (VLBA) + Green Bank Telescope (GBT) campaign estimated the size at 1.31×0.64 mas cm^{-2} , oriented 78° east of north [Bower et al., 2006].

An accurate extrapolation of the scattering kernel to 1.3 mm is important for the EHT scattering-mitigation strategy Fish et al. [2014] which aims to deblur the scattered image through a deconvolution procedure. However as this extrapolation is over at least an order of magnitude, any small systematic error in the original measurement can significantly effect the 1.3 mm extrapolated parameters. A recent review of VLBI observations of Sgr A*

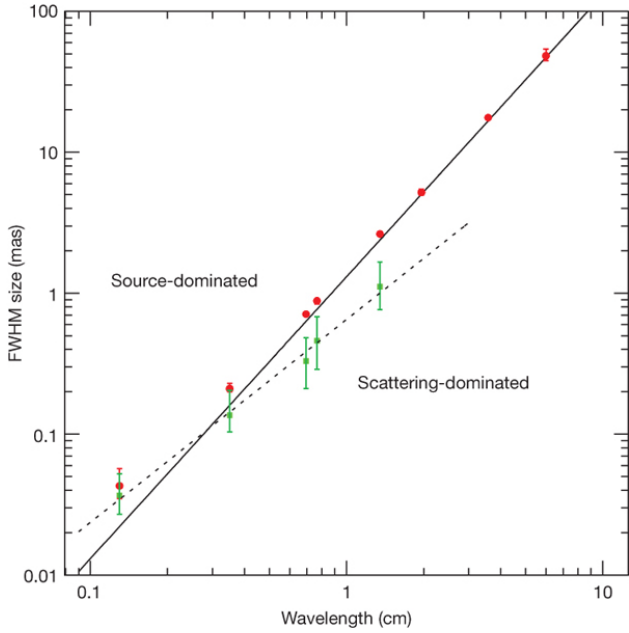


Figure 2.2: The λ^2 dependence of scattering kernel size is shown by the solid line. This has been derived from measurements made at $\lambda > 17$ cm Bower et al. [2006]. The dotted line shows the derived intrinsic source size which scales as $\lambda^{1.44}$. This was derived from measurements in the wavelength range, $2 \text{ cm} < \lambda < 1.3 \text{ mm}$ [Doeleman et al., 2008]. The red circles show major-axis observed sizes of Sgr A* and the green points show the derived intrinsic major-axis size. This plot was reproduced from Doeleman et al. [2008].

Psaltis et al. [2015] has noted that there are significant inconsistencies between different measurements. The authors used a Bayesian methodology to re-analyse the datasets resulting in increased uncertainties as shown in table 2.1. The minor axis has a much larger uncertainty than the major axis due to the limited north-south coverage of the VLBA array.

The blurring effect can be explained by the simple scattering model introduced in Sec. 2.2.1. Recall, that in the strong scattering regime EM waves propagate from coherent patches with linear size $\sim r_0$, assuming a point source. Each patch will emit light coherently into a single-slit diffraction cone of angular size $\theta_{\text{scatt}} \sim \lambda/r_0$. An observer will hence be illuminated by

Table 2.1: A re-analysis of VLBI observations of Sgr A* by Psaltis et al. [2015] has yielded revised estimates of the parameters associated with the Gaussian scattering kernel. Note that the position angle is measured East of North.

major axis FWHM (mas/cm ⁻²)	1.32	0.04
minor axis FWHM (mas/cm ⁻²)	0.82	0.21
position angle (°)	77.8	9.7

many patches spanning θ_{scatt} , yielding a blurred and broadened image, with projected size on the screen equal to the *refractive scale*,

$$r_{\text{ref}} = \theta_{\text{scatt}} D_{\text{os}} = r_F^2/r_0. \quad (2.20)$$

r_{ref} is the third fundamental length scale in the strong scattering regime and is associated with the refractive timescale,

$$t_{\text{ref}} = r_{\text{ref}}/v, \quad (2.21)$$

where v is bulk, transverse velocity of the screen. We can calculate r_0 given the FWHM of θ_{scatt} through the more precise relation

$$\theta_{\text{scatt}} = \frac{2\sqrt{2 \ln 2}}{2\pi} \lambda/r_0(M + 1) \quad (2.22)$$

where $M = D_{\text{os}}/R$ is the magnification factor and R is the source-screen distance. The magnification factor is a correction to the model introduced in Sec. 2.2.1 when $R \approx \infty$ no longer holds and should be used when calculating distances in the observer plane [Goodman and Narayan, 1989]. The location of the scattering medium was originally thought to be in the Galactic Centre itself (within ≤ 1 kpc). However, observations of a newly discovered pulsar, SGR J1745-29, indicate that the scattering screen is located at a distance $D_{\text{os}} = 5.8 \pm 0.3$ kpc, within the Scutum spiral arm [Bower et al., 2013]. Using Eq. 2.22 and the parameters given in table 2.1, we find that the major

axis of the coherence length at 1.3 mm, $r_0 \approx 3100$ km (i.e. 0.25 Earth diameters).

Recent EHT and space-VLBI observations have been extending their focus past well-studied Gaussian convolution effect of ISM scattering and onto the presence of stochastic scattering-induced substructure [e.g. Fish et al., 2016, Johnson et al., 2016]. To understand this phenomenon, we must first develop the theory to be sensitive to averaging over time, frequency and extended structure.

Strong scattering can be further subdivided into *snapshot*, *average* and *ensemble-average* regimes [Narayan and Goodman, 1989, Goodman and Narayan, 1989]. To understand the different regimes, remember that for each point on the source, the observer sees emission from coherent patches of area $A_{\text{strong}} \sim \pi r_0^2$ over a total area $A_{\text{ref}} \sim \pi r_{\text{ref}}^2$. The diffraction cones from each of the patches will interfere, resulting in a *diffractive scintillation* pattern, analogous to the classic multi-slit experiment.

In the *snapshot regime*, a compact source is observed with a narrow bandwidth and over a short time integration. This yields a single realisation of the diffractive scintillation pattern. By averaging over many snapshots, diffractive scintillation is quenched. This occurs if the source size θ_{src} is much larger than the diffractive scale $\theta_{\text{src}} \gg r_0/D_{\text{os}}$; if the fractional bandwidth $\delta\nu/\nu$ is much larger than the decorrelation bandwidth $\delta\nu/\nu \gg \delta\nu_{\text{dc}}/\nu \approx (r_0/r_F)^2$ [Narayan, 1992]; or if the integration time t_{int} is much larger the diffractive timescale $t_{\text{int}} \gg t_0 = r_0/v$, where v is the relative velocity between screen, source and observer. This regime is hence only accessible through observations of compact objects like pulsars. This regime is also reached when stars are viewed with the naked eye, hence the appearance of ‘twinkling’. On a side note, observations in this regime can be used to probe the source with angular resolution $\sim \lambda/r_{\text{ref}}$ [e.g. Gwinn et al., 2012]. This is because the scattering screen is essentially a lens of diameter $\approx r_{\text{ref}}$.

In the *average regime*, diffractive scintillation has been averaged over,

however there still exists scintillation over scales comparable to the size of the scattered image of a point source $\sim r_{\text{ref}}$, termed *refractive scintillation*. Phase fluctuations on this scale act like a weak lens to focus or defocus the λ/r_0 scale diffraction cones in the direction of the observer. For a point source this would lead to weak flux variations in the total flux [Narayan, 1992]. We will show later that refractive scintillation leads to the presence of substructure for a resolved scatter-broadened source. In contrast to diffractive scintillation, refractive scintillation is much more difficult to average over. Typically the refractive time scale $t_{\text{ref}} = r_{\text{ref}}/v$ is on the order of weeks to months for scattering towards the Galactic Centre i.e. longer than an observation campaign; the fractional decorrelation bandwidth is on the order of unity $\delta\nu_{\text{dc}}/\nu \sim 1$ (c.f. EHT $\sim 1 - 10\%$; and the source has to be much larger than the image of a scattered point source $\theta_{\text{src}} \gg \theta_{\text{scatt}} \sim 10\mu\text{-arcsec}$ at $\lambda = 230$ GHz. Continuing the analogy with viewing the sky with the naked eye, this regime is reach when planets are viewed, hence the diminished variability ('twinkling').

In the *ensemble-average regime*, both diffractive and refractive scintillation have been averaged over. It is in this regime when the scattering is equivalent to Gaussian convolution which is deterministic and not time variable.

A recent theoretical work [Johnson and Gwinn, 2015] has derived a useful approximation of the resolved scattered image I_{ss} in the average regime,

$$I_{\text{ss}}(\mathbf{x}) \approx I_{\text{src}}(\mathbf{x} + r_{\text{F}}^2 \nabla \phi(\mathbf{x})), \quad (2.23)$$

where ∇ is the directional derivative. Here we have used the same two-dimensional coordinate system, indexed by \mathbf{x} to describe the source, screen and observer planes which are considered to be aligned along the vertical axis. The scattered image I_{ss} is approximated by a ‘reshuffling’ of the source image I_{src} . As $|\nabla \phi| \sim 1/r_0$, the magnitude of the translation of points on $I_{\text{src}} \sim r_{\text{ref}} \sim 10 \mu\text{-arcsec}$ in the case of Sgr A* at 1.3 mm.

Even though $\phi(\mathbf{x})$ is only coherent to $\sim r_0$, $\nabla\phi(\mathbf{x})$ remains spatially coherent over much larger scales. The autocovariance of the phase derivative can be related to the structure function [Johnson and Gwinn, 2015]

$$\langle [\partial_x \phi(\mathbf{x}_0)][\partial_x \phi(\mathbf{x}_0 + \mathbf{x})] \rangle = \partial_x^2 D_\phi(\mathbf{x}). \quad (2.24)$$

A generalised structure function [Tatarskii, 1971, Narayan and Goodman, 1989] is quadratic (r^2) at small scales ($r << r_{\text{in}}$), Kolmogorov in the range $r_{\text{in}} < r < r_{\text{out}}$ and constant for $r > r_{\text{out}}$. Taking the simplifying case of $r_{\text{in}} \gg r_0$ and $r_{\text{in}} < r < r_{\text{out}}$, D_ϕ becomes [Johnson, 2013],

$$D_\phi = \frac{2}{\beta} \left(\frac{r_{\text{in}}}{r_0} \right)^{2-\beta} \left(\frac{r}{r_0} \right)^\beta, \quad (2.25)$$

and,

$$\partial_r^2 D_\phi(r) \propto r^{\beta-2}. \quad (2.26)$$

Therefore in the Kolmogorov regime ($\beta = 5/3$), the coherence of image shift relative to the refractive scale $\propto (r/r_0)^{-1/3}$. Therefore, even though $\phi(\mathbf{x})$ is only coherent to $\sim r_0$, $\nabla\phi(\mathbf{x})$ remains spatially coherent over much larger scales, leading to the presence of refractive substructure [Johnson and Gwinn, 2015].

A recent observation of Sgr A* at 3.5 mm by the VLBA+LMT [see Fig. 2.2 Ortiz-León et al., 2016] has measured non-zero closure phases on its longest baselines. However it was also shown in the data analysis that the measured values are consistent with expectation refractive scintillation assuming a circular Gaussian source of FWHM = 130 $\mu\text{-arcsec}$, which is the fitted size of the major axis of the intrinsic source emission. Another observation at 1.3 cm shows flux amplitude variability due to scattering substructure $\Delta S \sim 10$ mJy [Gwinn et al., 2014]. Predictions for $\lambda = 1.3$ mm show ~ 60 mJy for long East-West baselines and ~ 25 mJy for long North-South baselines [Johnson and Gwinn, 2015], assuming a Gaussian source of FWHM = 40 $\mu\text{-arcsec}$.

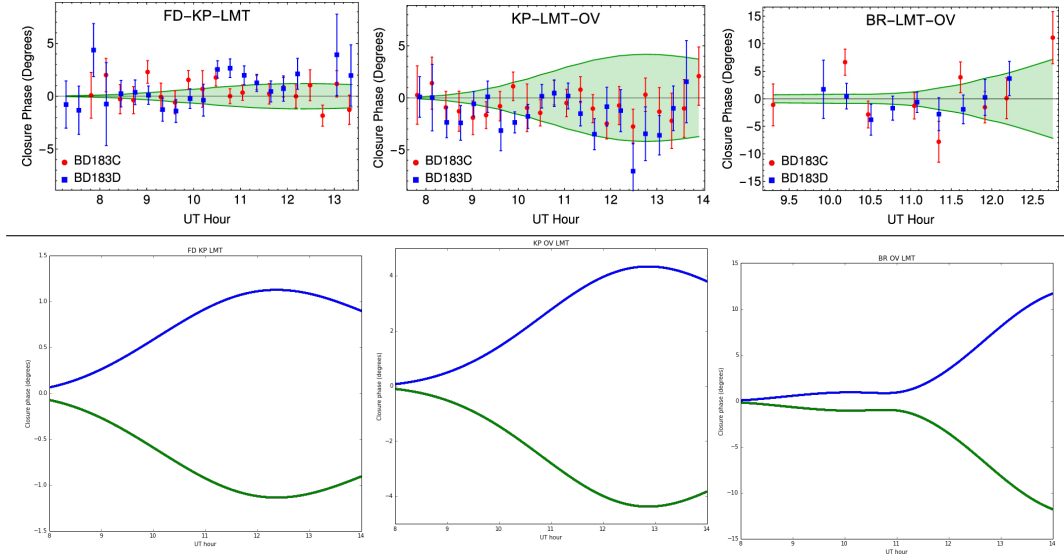


Table 2.2: **Top panel :** Closure phases recorded in a VLBA + LMT observation of Sgr A * at $\lambda = 3.5$ mm [Ortiz-León et al., 2016]. The data points are shown as red circles and blue squares and are only distinguished by the calibrator used. The green envelopes show the 1σ closure phase prediction induced by scattering-induced substructure. The prediction was generated by simulating interferometric observations of 500 independent realisations of a scattered circular Gaussian with FWHM = $130 \mu\text{-arcsec}$. Reproduced from Ortiz-León et al. [2016]. **Bottom panel :** Reproduction of the above result using the MEQSILHOUETTE simulator using 50 independent realisations of the scattering screen. The success of the reproduction confirms the functionality of a large section of the simulator.

Distinguishing intrinsic source and ISM substructure and variability is an interesting challenge. Observations at mm-wavelengths have revealed deviations from the λ^2 scattering scaling law, see Fig. 2.2. This is interpreted as due to the presence of intrinsic source structure and has been fitted with a power-law with an exponent of 1.34 ± 0.01 [Lu et al., 2011]. This has enabled the constraint of various theoretical models Bower et al. [2006], excluding advection-dominated accretion flows [(ADAF), Narayan and Yi, 1995] and Bondi-Hoyle accretion [Melia, 1994]. However observations ex-

tending over month timescales are required to properly sample the larger scale inhomogeneities and even with multiple epoch observations, it can be difficult to distinguish source and scattering characteristics [Macquart and Bower, 2006]. The developments in scattering theory presented above provide a robust mechanism for quantifying refractive effects. This could allow a decoupling without sampling a refractive ensemble but significant assumptions are always made on the source model.

2.2.3 Troposphere

The coherence and intensity of millimetre wavelength electromagnetic waves are most severely deteriorated in the lowest atmospheric layer, the troposphere which extends up to an altitude of $7 - 10$ km above sea level and down to a temperature $T \sim 218$ K [Thompson et al., 2001]. The troposphere is composed of a number of different components including primary gases N_2 and O_2 , trace gases e.g. water vapour and CO_2 , as well as particulates of water droplets and dust. The rest of this section will explore the tropospheric corruption for the mm-VLBI case beginning with insights from the fundamentals of electromagnetic propagation, followed by a review of atmospheric corruptions in the sub-mm regime. We then firm up our theory with a discussion on atmospheric radiative transfer and atmospheric turbulence.

Propagation fundamentals

Consider a quasi-monochromatic wave passing through a linear medium,

$$E_\nu(x, t) = E_0 \exp^{i(kn_\nu x - 2\pi\nu t)}, \quad (2.27)$$

where $k = 2\pi\nu/c$ is the propagation constant in free space and $n = n_{\text{R}} + jn_{\text{I}}$ is the complex index of refraction. Note that we will occasionally omit the frequency dependence of n and related quantities to simplify the notation. If

n_I is nonzero, the electric flux I will decay exponentially

$$I = E E^* = E_0^2 \exp(-\tau), \quad (2.28)$$

where τ is called the opacity or optical depth and is related to the absorption coefficient, $d\tau = \kappa dx$ where $\kappa = 4\pi\nu n_I/c$. If $n_R > 1$ the phase velocity of the EM wave will decrease, $v_p = c/n_R$, which results in a time delay. The time delay due to the troposphere, \tilde{t} and opacity τ can be calculated simultaneously,

$$\tilde{t} + i\tau/4\pi\nu = 1/c \int_{path} d\mathbf{s} (n_\nu(\mathbf{s}) - 1). \quad (2.29)$$

In the interferometric context opacity and time delay are often viewed independently. However, the electric field is real and causal which imposes restrictions on the complex refractive index. Specifically n_R and n_I contain the same information and can be interchanged via the Kramers-Kronig relations.

Absorption is accompanied by emission and for a medium in local thermodynamic equilibrium, Kirchoff's law states that

$$\frac{\epsilon_\nu}{\kappa_\nu} = B_\nu(T), \quad (2.30)$$

where $\epsilon_\nu = dI_\nu/dx$ is the emission coefficient and $B_\nu(T)$ is the Planck function. Hence the absorbing molecules are also emitters, and so non-zero opacity will lead to both absorption and emission, the latter of which will be seen by the receiver as an increased sky noise component, and hence an increase in total system temperature/noise. Therefore opacity, time delay and atmospheric noise are interrelated and should be simulated consistently. On a side note these relations allow for phase calibration using measurements of sky emission via Water Vapour Radiometry (WVR) [e.g. Carilli and Holdaway, 1999].

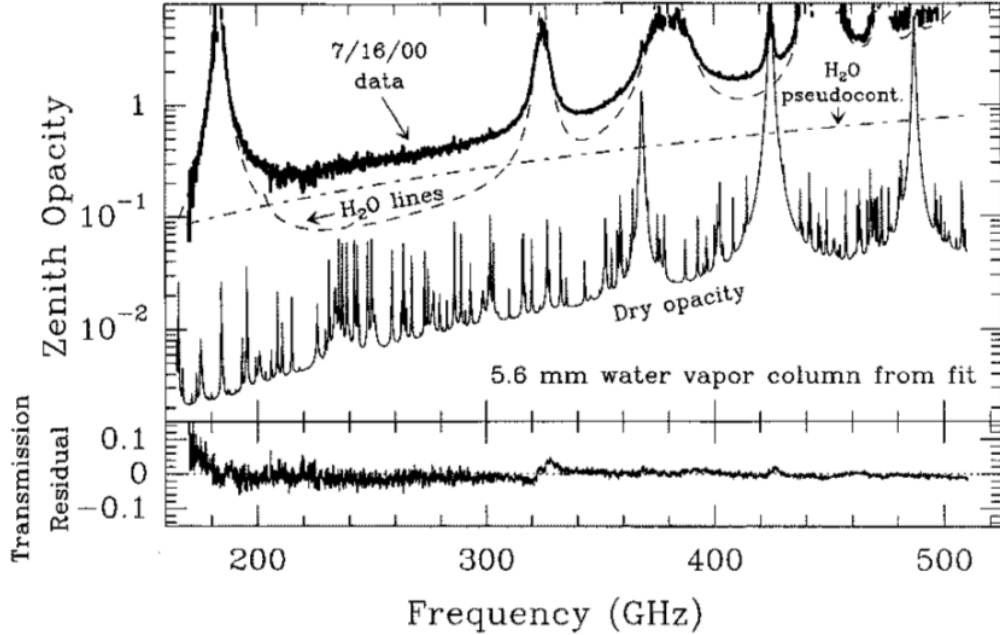


Figure 2.3: Recorded zenith absorption spectrum in the 160–520 GHz range, taken on Mauna Kea at an altitude of ≈ 4000 m. The data has been fit to a sum of H₂O lines, an H₂O pseudo-continuum and dry absorption lines. The model has been generated using the ATM code (see section 2.2.3), with the bottom panel showing the residuals. Here ‘dry’ refers to all atmospheric constituents except H₂O. Reproduced from Pardo et al. [2001]

Atmospheric corruptions in the (sub-)mm regime

An analysis of the absorption spectrum in the GHz range (Fig. 2.3), shows that it is dominated by transitions of H₂O and O₂ as well as a pseudo-continuum opacity which increases with frequency. The pseudo-continuum opacity is due to the cumulative effect of the far wings of a multitude of pressure-broadened water vapour lines above 1 THz [Carilli and Holdaway, 1999]. At 230 GHz the absorption is typically 5 – 10% at the best sites (e.g. Mauna Kea), during good weather .

In contrast to the dry atmospheric components, water vapour mixes

poorly and its time-variable spatial distribution induces rapid fluctuations in the time delays \tilde{t} above each station. The phase error for a baseline (1,2) where antenna 1 is the reference will be

$$\delta\phi(t, \nu) = 2\pi/\nu(\tilde{t}_2(t, \nu) - \tilde{t}_1(t, \nu)). \quad (2.31)$$

The water vapour column density is measured as the depth of the column when converted to the liquid phase and is referred to as the precipitable water vapour (PWV). PWV is directly proportional to the time delay and hence the phase delay,

$$\delta\phi \approx \frac{12.6\pi}{\lambda} \times w, \quad (2.32)$$

where w is the depth of the PWV column [Carilli and Holdaway, 1999] and an atmospheric temperature $T = 270$ K has been assumed. This relationship between phase and water vapour content has been experimentally verified [Hogg et al., 1981]. At 230 GHz, the change in PWV needed to offset the phase by 1 rad is $\Delta w \approx 0.03$ mm (again, assuming $t = 270$ K).

This sensitive dependence of phase coherence on atmospheric stability is aggravated by three factors. Firstly, antenna elevation angles are typically fairly low for EHT observations which increases the atmospheric path length. Secondly, as stations are far apart ($\gg 100$ km $\gg r_{\text{out}}$) the atmospheric variations are uncorrelated between stations, this increases visibility decoherence as atmospheric variations appearing in both terms of equation 2.31 fall away. Thirdly, observing with few stations gives less constraints on unknown complex gains and therefore a smaller fraction of retrievable intrinsic information [Thompson et al., 2001].

Radiative transfer

The problem of radiative transfer through a static atmosphere is well described and implemented by the Atmospheric Transmission at Microwaves

(ATM) software [Pardo et al., 2001]. ATM has been incorporated into MEQSIL-HOUETTE to provide a fast and sophisticated procedure to calculate average opacities, sky brightness temperatures and time delays. Here we provide a brief summary of the theory underpinning the package but refer the reader to Pardo et al. [2001] for more detail. ATM is commonly used in the Atacama Large Millimeter Array (ALMA) community [e.g. Curtis et al., 2009, Nikolic et al., 2013] and has been tested with atmospheric transmission spectra taken on Mauna Kea [Serabyn et al., 1998].

We start from the unpolarised radiative transfer equation, which is unidirectional in the absence of scattering,

$$\frac{dI_\nu(s)}{ds} = \epsilon_\nu(s) - \kappa_\nu(s)I_\nu(s), \quad (2.33)$$

where s is the coordinate along the signal path through the atmosphere. We assume local thermodynamic equilibrium (LTE) which should hold as the collisional timescale is much smaller than the time for spontaneous emission for all but the highest part of the atmosphere. Applying equation 2.30, multiplying by $\exp(-\tau_\nu)$ and integrating from the top of the atmosphere ($s = 0$) yields,

$$I_\nu(s) = I_\nu(0)e^{-\tau_\nu(0,s)} + \int_0^s B_\nu(s')e^{-\tau_\nu(s',s)}\kappa_\nu(s')ds', \quad (2.34)$$

where s' is a dummy variable in the same direction as s and $\tau_\nu(0,s) = \int_0^s k_\nu(s')ds'$. $I_\nu(0)$ is normally taken as the radiance from the Cosmic Microwave Background (CMB). To calculate the $I_\nu(s)$, $\tau(s)$ and complete the above integral, requires κ_ν as a function of altitude and frequency. The time delay \tilde{t} can be calculated from τ using the Kramers-Kronig relations.

A general equation to determine the absorption coefficient for a transition between a lower l and upper u states is given in Pardo et al. [2001]. Here we merely point out that it should be proportional to the energy of the photon, $h\nu_{l \rightarrow u}$, the transition probability or Einstein coefficient, $B_{l \rightarrow u}$, the line-shape,

$f(\nu, \nu_{l \rightarrow u})$ and the number densities N of electronic populations. Line profiles which describe pressure broadening (perturbations to the Hamiltonian due to the presence of nearby molecules) and Doppler broadening are used. The condition of detailed balance further requires that decays from the upper state are included yielding, $g_u B_{u \rightarrow l} = g_l B_{l \rightarrow u}$, where g is the degeneracy of the electronic state. Putting this together we find,

$$\kappa(\nu)_{l \rightarrow u} \propto h\nu B_{l \rightarrow u} \left(\frac{N_l}{g_l} - \frac{N_u}{g_u} \right) f(\nu, \nu_{l \rightarrow u}), \quad (2.35)$$

where the Einstein coefficients are calculated from the inner product of the initial and final states with the dipole transition operator,

$$B_{l \rightarrow u} = \frac{2\pi}{3\hbar^2} | \langle u | \mu | l \rangle |^2, \quad (2.36)$$

where $|u\rangle$, $|l\rangle$, $|\mu\rangle$ are the wavefunctions of upper and lower states and the dipole transition operator respectively. The number densities of the two states, N_u and N_l in local thermodynamic equilibrium (LTE) are simply related to the local number density and temperature via Boltzmann statistics,

$$\frac{N_n}{N} = g_n \frac{\exp -\frac{E_n}{kT}}{Q}, \quad (2.37)$$

where the partition function, $Q = \sum_i g_i \exp -E_n/kT$. Transition lines at radio wavelengths result from rotational state transitions. To calculate the inner product given in equation 2.36, operators which describe linearly symmetric rotors (e.g. O₂, CO) and asymmetric rotors are used. The asymmetric rotations are decomposed into three principal rotation axes with differing rotational constants governing each axis. Rotational constants were measured by the authors as well as drawn from a variety of literature. Partition functions and transition probability are calculated using approximations taken from the literature.

Far wing broadening of H₂O lines > 1.2 THz extends to lower frequencies

and is not completely represented by the line-shape used. This is believed to be due to self-self collisions of water molecules. Additionally there are terms from the dry atmosphere related to transient dipoles and Debye absorption which are not represented in the line-shape. To correct for these effects, two pseudocontinua are used. These are modelled as a power law dependence on frequency, temperature and the molecular densities.

The treatment of radiative transfer in ATM, and hence MEQSILHOUETTE, aims to be as physical as possible whilst still being able to describe key phenomenological features e.g. the pseudocontinuum opacity. The efficacy of the accuracy provided by this implementation is in the ability to contribute to a quantitative determination of the uncertainties inherent in mm-VLBI.

Turbulent phase fluctuations

“Visibility phase instability $\delta\phi(t)$ due to tropospheric turbulence is a fundamental limitation to producing high dynamic range, high fidelity, science-quality maps with a mm-VLBI array [Thompson et al., 2001]. The coherence time-scale is typically too rapid ($\lesssim 10$ s) for fast switching calibration, so other calibration procedures (e.g. water vapour radiometry, paired antennas, and/or self-calibration) must be performed. Self-calibration is the most commonly used but is limited by the integration time needed to obtain adequate SNR to fringe-fit (see section 2.1.2). Phase decoherence often leads to the use of closure quantities to perform model fitting [Doeleman et al., 2001, Bower et al., 2004, Shen et al., 2005], and causes a decrease in measured flux due to incoherent complex averaging.”

[Blecher et al., 2016]

In this section we will review and develop the weak scattering theory introduced earlier which will culminate in a formulation for the simulation

of tropospheric phase turbulence seen by a mm-VLBI array. How this formulation is implemented and fits into the broader atmospheric simulation framework will be discussed in section 3.2.2.

Following from section 2.2.1, we model the statistics of $\delta\phi(t)$ with a thin, frozen, Kolmogorov-turbulent phase screen moving with a bulk velocity, v . However, the turbulent layer has a finite width Δh and outer scale r_{out} and both Kolmogorov theory and measurement [Fig. 2.4, Coulman, 1985, Treuhhaft and Lanyi, 1987, Carilli and Holdaway, 1997] show that β should move continuously through approximately three regimes,

$$\beta = \begin{cases} 5/3 & \text{if } r < \Delta h, \\ 2/3 & \text{if } r > \Delta h, \\ 0 & \text{if } r > r_{\text{out}}. \end{cases} \quad (2.38)$$

In Fig. 2.4 we can see estimations of $\Delta h \approx 1$ km and $r_{\text{out}} \approx 6$ km. We will show later that even though we are working with a VLBI array, our implementation falls into the $r \ll \Delta h$ regime.

“We set the height h of the screen at the water vapour scale height of 2 km above ground. At 1.3 mm, the Fresnel scale is $r_F \approx 0.45$ m and experiments show annual variations of $r_0 \sim 50 - 500$ m above Mauna Kea [Masson, 1994] and $r_0 \sim 90 - 700$ m above Chajnantor [Radford and Holdaway, 1998], where both sites are considered to have excellent atmospheric conditions for (sub)millimetre astronomy. As $r_F < r_0$, this is an example of weak scattering.

The required field-of-view (FoV) of a global mm-VLBI array is typically $FWHM < 1$ marcsec or $\sim 10 \mu\text{m}$ at a height of 2 km, which is roughly 7-8 orders of magnitude smaller than the tropospheric coherence length. The tropospheric corruption can therefore be considered constant across the FoV and, from the perspective of the Measurement Equation, modeled as a diagonal

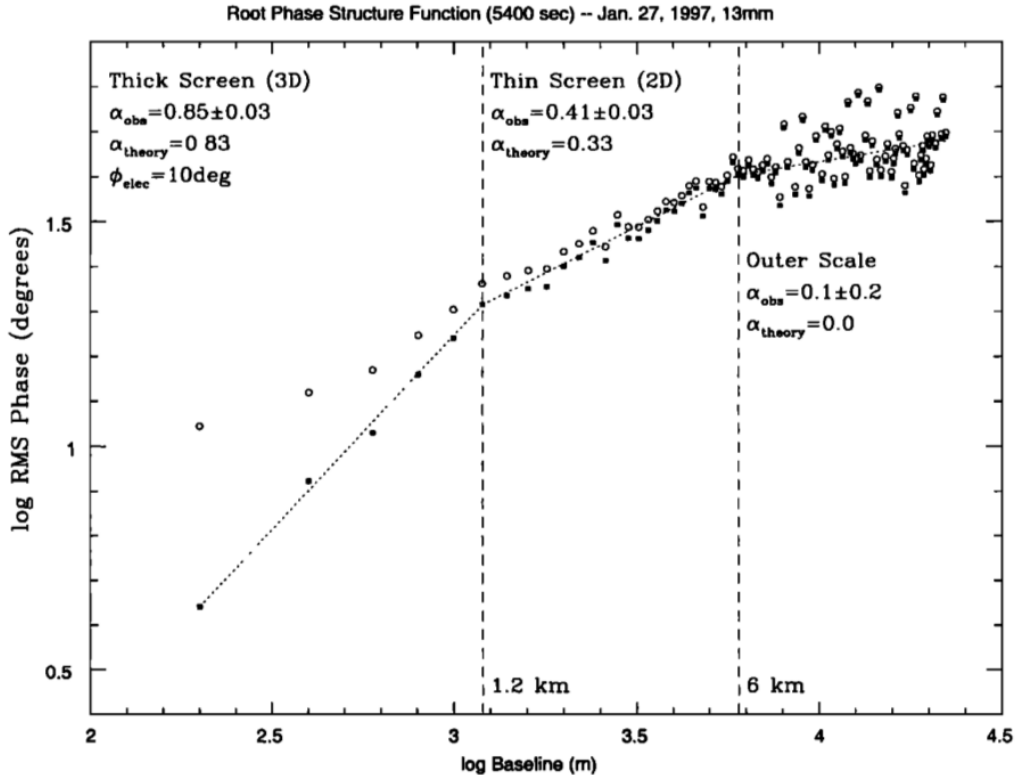


Figure 2.4: A log-log plot of RMS visibility phase versus baseline length for an observation of 1 Jy source 0748 + 240 with VLA at 22 GHz over a 90 min duration. The open circles show RMS phase as measured whereas the solid squares show the same values with a constant thermal noise contribution of 10° subtracted in quadrature. Note that the measured and theoretical Kolmogorov turbulent exponent β changes with distance on the phase screen as the viewing configuration transitions from a thick screen ($\beta_{\text{theory}} = 5/3$) to a thin screen ($\beta_{\text{theory}} = 2/3$) at $r \approx 1$ km and from a thin screen to completely uncorrelated regime ($\beta = 0$) beyond the outer scale at $r \approx 6$ km. Although these regimes appear distinct, there is continuous variation between them. Reproduced from Carilli and Holdaway [1997]

Jones matrix per time and frequency interval. As VLBI baselines are much longer than the coherence length, $|\mathbf{b}| \geq 1000 \text{ km} \gg r_0$, the phase screen at each site must be simulated independently. This assumption only holds for VLBI baselines and the framework needs to be extended to simulate the effects of turbulence on individual phased arrays stations (e.g. SMA) and short ($< 10 \text{ km}$) baselines (e.g. JCMT - SMA).” [Blecher et al., 2016]

In principle, this could be approximated by assuming a time-variable phase efficiency for the phased array stations, however this is for future work.

“Our aim then is to produce a phase error time sequence $\{\delta\phi(t_i)\}$ for each station which is added to the visibility phase. We invoke the frozen screen assumption and write the structure function as a function of time, $D(t) = D(r)|_{r=vt}$. The temporal structure function $D(t)$ provides an efficient route to sample the variability of the troposphere at the typical integration time of the dataset, $t_{\text{int}} \sim 1 \text{ sec}$.

The temporal variance of the phase is a function of the temporal structure function, and accounting for time integration yields [see Treuhhaft and Lanyi, 1987, B3]

$$\sigma_\phi^2(t_{\text{int}}) = (1/t_{\text{int}})^2 \int_0^{t_{\text{int}}} (t_{\text{int}} - t) D_\phi(t) dt. \quad (2.39)$$

Assuming power-law turbulence and integrating yields,

$$\sigma_\phi^2(t_{\text{int}}) = \left[\frac{1}{\sin \theta(\beta^2 + 3\beta + 2)} \right] \left(\frac{t_{\text{int}}}{t_0} \right)^\beta, \quad (2.40)$$

where $t_0 = r_0/v$ is the coherence time when observing at zenith and $1/\sin \theta$ is the approximate airmass which arises as $D_\phi \propto w$. As $r \ll \Delta h$, where Δh is the thickness of the turbulent layer, an thin screen exponent of $\beta = 5/3$ is justified [Treuhhaft and Lanyi,

1987].”

[Blecher et al., 2016]

Hence we can write $\{\delta\phi(t_i)\}$ as a Gaussian random walk for each antenna, as this is essentially a random walk on the phase screen. At mm-wavelengths, the spectrum of water vapour is non-dispersive up to a few percent [Curtis et al., 2009] and so we can assume a simple linear scaling across the bandwidth, however note that phase dispersion is taken into account in the mean atmospheric component.

“Phase fluctuations $\delta\phi(t)$ can also be simulated by taking the inverse Fourier transform of the spatial phase power spectrum. However this approach is much more computationally expensive, e.g. for an observation length t_{obs} involving $N_{\text{ant}} = 8$ independent antennae with dish radii $r_{\text{dish}} = 15$ m, wind speed $v = 10$ m s⁻¹ and pixel size equal to r_F , the number of pixels $N_{\text{pix}} \approx N_{\text{ant}} t_{\text{obs}} r_{\text{dish}}^2 / (v r_F^3) \sim 10^8$. Additionally, due to fractal nature of ideal Kolmogorov turbulence, the power spectrum becomes unbounded as the wavenumber approaches zero which makes it difficult to determine the sampling interval of the spatial power spectrum [Lane et al., 1992].”

[Blecher et al., 2016]

2.2.4 Instrumental

All instruments suffer from both systematic and stochastic errors, the characterisation of which determines the measurement accuracy and precision respectively. In this section we explore thermal noise (stochastic) and antenna pointing errors (systematic).

Thermal Noise

The level of thermal noise of the measurement defines the absolute limit on the sensitivity of the interferometer to detect a source and also to distinguish fine source characteristics. Closure quantities are especially prone to high levels of thermal noise as several visibilities are multiplied with one another. The thermal noise of an interferometer can be derived by correlating the thermal noise of two antennae [Wrobel and Walker, 1999]. The RMS thermal noise of an interferometer $\{i, j\}$, over a bandwidth $\Delta\nu$, for a single polarisation and over an integration time t_{int} is given by

$$\Delta S_{ij} = \frac{1}{\eta_s} \sqrt{\frac{SEFD_i SEFD_j}{2\Delta\nu t_{\text{int}}}}, \quad (2.41)$$

where η_s is the system efficiency and $2\Delta\nu t_{\text{int}}$ is the number of independent samples. The $SEFD$ is a measure of the sensitivity of an antenna, accounting for the efficiency, collecting area and thermal noise and is defined as the flux density of a source with the same power,

$$SEFD = 2k_B T_{\text{sys}} / (\eta_a A), \quad (2.42)$$

where A is the antenna area, η_a is the antenna efficiency, T_{sys} is the system temperature and the factor $\frac{1}{2}$ accounts for only sampling 1 polarisation.

As the RIME was formulated for a thermal noise-free measurement, we do not apply this corruption as a multiplicative matrix but rather an additive matrix,

$$\mathbf{V}_{pq} = \mathbf{G}_p \mathbf{X}_{pq} \mathbf{G}_q^H + \mathbf{N}_{pq}, \quad (2.43)$$

where each component of N_{pq} is sampled from a complex-valued Gaussian distribution of mean and variance, $|N_{pq}| \sim (0, \Delta S_{ij}^2)$.

Antenna Pointing

“All antennas suffer pointing errors to some degree due to a variety of factors including dish flexure due to gravity, wind and thermal loading, as well as drive mechanics. This corresponds to an offset primary beam, which should only translate to minor amplitude errors if the pointing error θ_{PE} is significantly smaller than the primary beam (i.e. $\theta_{\text{PE}} \ll \theta_{\text{PB}}$). In the Measurement Equation formalism, this offset can be represented by a modified (shifted) primary beam pattern in the E -Jones term [see Smirnov, 2011a]

$$\mathbf{E}_p(l, m) = \mathbf{E}(l_0 + \delta l_p, m_0 + \delta m_p), \quad (2.44)$$

where $\delta l_p, \delta m_p$ correspond to the directional cosine offsets.”

[Blecher et al., 2016]

This could be a problem for millimetre observations as the primary beam is narrow. For example, at an observing frequency of 230 GHz, the primary beam of a 30 m dish is $\theta_{\text{PB}} \sim 10$ arcsec. The typical pointing budget for millimetre stations are $\theta_{\text{PE}} \sim 1$ arcsec. Hence we have chosen to investigate the effect which pointing errors could have on mm-VLBI observables.

We identify two main classes of pointing error. Firstly, an antenna tracking a source could suffer a slow, continuous time-variable pointing error associated with the tracking error σ_{track} . Physically, this could be attributed to changes in wind, thermal and gravitational loading which all change with telescope pointing direction and over the course of a typical few hour observation. Using the MEQTREES software package, such behaviour has been demonstrated to occur with the Westerbork Synthesis Radio Telescope [Smirnov, 2011d,c, WSRT,]).

Secondly, whilst a stationary phase centre is tracked, the pointing error should evolve slowly and smoothly, however, in mm-VLBI observations the phase centre is often shifted to another source/calibrator. This would

cause the pointing error to change abruptly, with an absolute pointing error $\sim \sigma_{\text{abs}}$. Source/calibrator change is scheduled every 5-10 minutes in a typical millimetre observation. The point is that even though EHT will be able to determine the pointing offset when observing a calibrator with relatively well-known structure, when the antennas slew back to a source (e.g. Sgr A*) with less certain or variable source structure, the pointing error could change significantly. This is exacerbated by the scarcity of mm-wavelength calibrators, which are often widely separated from the source.

Chapter 3

Software implementation

3.1 Design objectives

Our primary aim is to test and research mm-VLBI calibration, imaging and parameter estimation algorithms/strategies through the construction of a synthetic data simulation framework. To address the many questions within the wide scope of this objective, one must be able to setup and run a diverse set of experiments within the simulation framework. This places definite constraints on the software architecture. In particular, the framework should :

- enable the implementation of the dominant classes of signal corruption within a formalism which ensures consistency with the causal signal transmission chain,
- be compatible with time-variable GRMHD source models which are to be used as inputs,
- be organised in a modular structure so that it is flexible, extendable and could be incorporated into other interferometric algorithms or vice-versa e.g. a calibration or a parameter estimation algorithm,

- the modular structure should also enable the construction and execution of arbitrary observations.

3.2 Architecture and Workflow

In this section, we will review how the architechural design and workflow of the simulator has been designed to meet the above objectives. To fulfill the first objective, we cast signal corruptions in the RIME formalism (see section 2.1.1). This is not currently possible for the case of ISM-scattering, however we do apply it in the casually correct position in the signal transmission chain, with proper consider given to non-communitivity of elements. The implementation of each signal corruption is described in the following subsections. The remaining objectives fall into the realm of software design and will be discussed in this subsection.

We have chosen to write the high level simulation code using the `PYTHON` language. `PYTHON` is a general purpose language, is geared towards readability, and is well supported by a comprehensive library and wide user base, particularly within astronomy. Even though the higher level functionality is written in `PYTHON`, the bulk of the computational load is called through subroutines which are written in the more computationally efficient `C++` language.

We use the interferometric toolbox, `MEQTREES` [Noordam and Smirnov, 2010], which can simulate and calibrate radio interferometric data through evaluation of a user-defined RIME. The evaluation draws on directed-acyclic-graphs (or compute trees) where each element of the graph can process a multi-dimensional grid of values (typically specified along axes of ν and t). Although we have decided to construct a large portion of our RIME outside of `MEQTREES`, we call prebuilt `MEQTREES` RIMEs to augment our pipeline in two ways. Firstly to perform the Fourier transform to generate visibilities from the input sky model (FFT for fits files; DFT for parametric sources),

where degridding and interpolation steps are also called when the FFT is used. The second is to simulate the primary beam and antenna pointing error, which will be discussed later in this chapter. On a side note, use of MEQTREES and MEASUREMENT SET also lends itself to investigating a range of different techniques that are used in other areas of interferometry [e.g. Smirnov and Tasse, 2015].

Our data formats of choice are: FITS for image cubes and the MEASUREMENT SET¹ (MS) for visibilities. We use MS as our data format as it is directly accessible in PYTHON via the PYRAP library and is the data format used by MEQTREES. Although in the mm-VLBI subfield, other data formats are currently still more popular than the MS, i.e. FITSIDI, UVFITS or IOFITS, largely due to the lack of a fringer fitter in CASA. However, thanks to development at the Joint Institute for VLBI in Europe (JIVE), we expect this to change in CASA V5.

To create a flexible and modular structure necessary to be able to run a diversity of experiments, the software implementation is divided into 2 components:

- an object-oriented framework into which is programmed the logic of each individual step in the signal propagation chain,
- a driver script which initialises the most abstract class in the framework with the required inputs and determines the signal propagation chain relevant to that particular pipeline.

The conceptual flow diagram of one realisation of a MEQSILHOUETTE simulation pipeline is shown in Fig. 3.1. To emphasise, the framework is not restricted to this sequence of operations, allowing the exact pipeline to be quite general. Note that this diagram is not entirely accurate as antenna pointing errors are not compatible with the FITS sky model output by the ISM scattering module.

¹<https://casa.nrao.edu/Memos/229.html>

All inputs to the simulator are specified by a configuration file, containing a dictionary (see table 3.1 as an example), which is the sole input to the driver script. This dictionary contains everything needed by the pipeline to determine the particular observation configuration (frequency, bandwidth, start time, etc), which signal corruption implementation should be employed and where the sky model, station weather information and antenna table are located in the filesystem. The antenna table is in the MS format, and can readily be created or altered using the PYRAP library using the station coordinates. The primary sky model used is a time-ordered list of FITS images, where each image represents the source total intensity over a time interval $\Delta t_{\text{src}} = t_{\text{obs}}/N_{\text{src}}$, where t_{obs} is the observation length and N_{src} is the number of source images [Blecher et al., 2016]. Currently the pipeline only supports total intensity and the conversion of the pipeline to support full Stokes is discussed in section 4.2. A variation of the pipeline has also been written which uses a parametric source model consisting of Gaussians or point sources as the sky model. This functionality was needed for the simulation of pointing errors as the MEQTREES beams model does not support the FITS sky model.

The primary outputs of the pipeline are an interferometric dataset in MS format along with the closure phases and uncertainties and a dirty and/or deconvolved image. Closure phases and uncertainties are calculated in a model-dependent way as described by section 2.1.3. The modular structure of the pipeline allows for additional imaging and deconvolution algorithms to be easily appended to the final data processing steps. Noting that there are other data formats widely used in mm-VLBI, we make use of the CASA task for conversion to UVFITS. Similiarly other data products can be easily produced as needed e.g. polarisation ratios.

An important step to reproduce realistic observations is to be able create a comprehensive MS with arbitrary scan lengths, start times, channel and

Table 3.1: **Top section:** keywords of the input configuration dictionary used in a standard simulation similar to that depicted in Fig. 3.1 but without antenna pointing errors. The variable names have been expanded for clarity and keywords which have boolean values have written as questions. In practice, most of these keywords are preceded by an index, which allows this dictionary to be filter into several subdictionaries which can be easily passed to functions or classes. **Bottom section:** the headings of station weather table whose path is indicated in the input dictionary.

input fits folder path	antenna table path
station information file path	integration time
start time	channel width
no. scan	scan lag
elevation limit	no. channels
central frequency	observation length
apply ISM scattering?	ISM screen speed
no. ISM screens?	ISM N_{pix}
apply atmospheric attenuation?	add thermal noise?
apply atmospheric thermal noise?	apply tropospheric phase noise?
apply mean atmospheric time delays?	percentage tropospheric phase
output image pixel size	output image N_{pix}
<hr/>	
station	coherence time
sefd	pvw
ground pressure	ground temperature

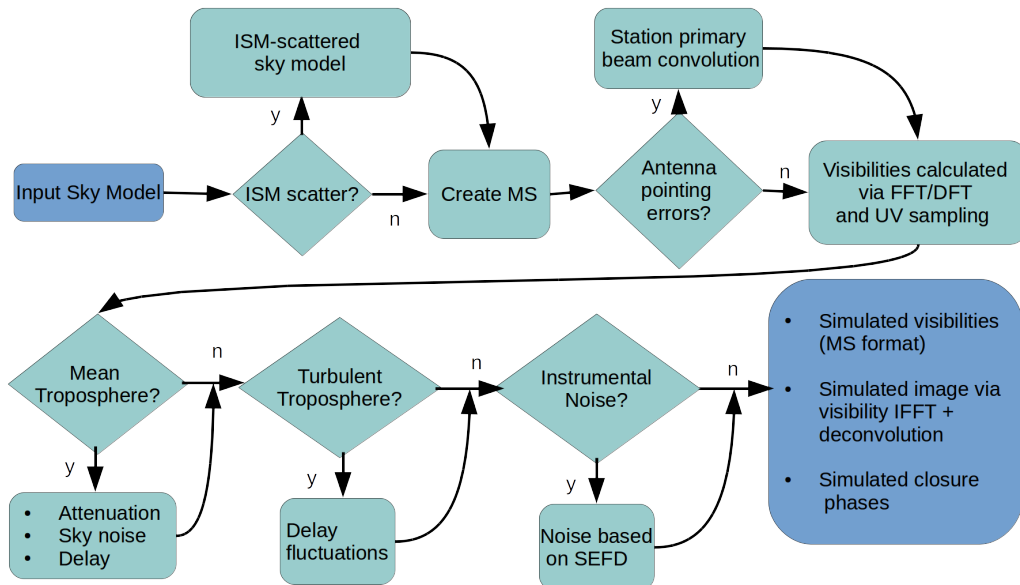


Figure 3.1: Flow diagram showing basic sequence of a MEQSILHOUETTE simulation pipeline. The specific sequence is determined by the driver script whereas the logic of each step is contained in an object-oriented framework. The details of the station information, observation strategy, tropospheric and ISM conditions are specified in a user-defined input configuration file. The pipeline is extendable, allowing any additional, arbitrary Jones matrices to be incorporated.

bandwidth structure. This is performed using the SIMMS² tool. SIMMS provides an easy to use command line interface to construct a general MS, given the appropriate antenna table. The call to SIMMS is located within the driver script.

In order to make the framework as clean and modular as possible we have made extensive use of object orientation, see Fig. 3.2 for a basic overview. The first major class, *SimpleMS*, was intended to abstract and modularise the MS and MS-only derived attributes (e.g. visibility data and station positions) and methods (e.g. functions to calculate station elevations and closure

²<https://github.com/radio-astro/simms>

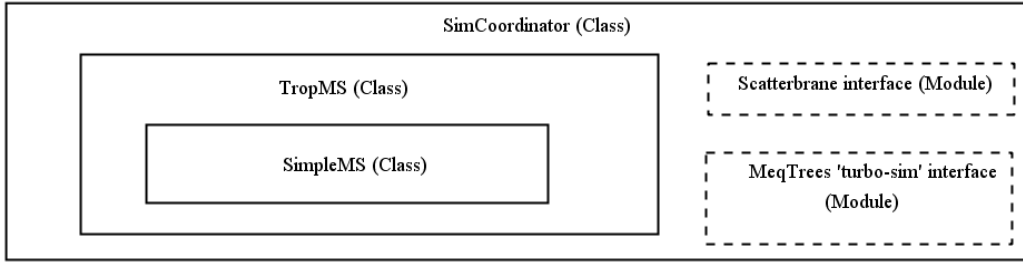


Figure 3.2: The basic class and module structure of the MEQSILHOUETTE implementation. Solid lines represent a class while dashed lines represent a module. The *SimCoordinator* class is initialised in the driver script.

phases) as well as expose these attributes and methods more efficiently than following PYRAP procedures which become verbose when used frequently. This is especially useful when accessing baseline-indexed quantities.

The second MS-related class, *TropMS*, handles the calculations relevant to tropospheric and thermal noise corruptions. This class is a child of *SimpleMS* and is initialised with weather and station information. Note that a child contains all the methods and attributes of its parent. This allows the tropospheric corruption implementation to use, whilst being separated from, the core MS functionality. The details of the tropospheric corruption are provided in section 3.2.2.

The third MS-related class, *SimCoordinator*, is a child of the *TropMS* class. *SimCoordinator* is designed to make a simulation, with an arbitrary experimental setup, easy and efficient to construct and execute on a high level. It is the only MS class directly initialised in the driver script and hence the low level functionality and attributes of its parents are abstracted from the user. In addition to inherited functionality, *SimCoordinator* can call the ISM-scattering task (see subsection 3.2.1), and MEQTREES simulation functionality.

Table 3.2: The list of the parameters, aside from the source model, needed to initialise and run SCATTERBRANE. Time variability is made possible as N_{pix} can be a 2-tuple (i.e. a rectangular screen can be created).

r_0	N_{pix}
r_{in}	principal angle
r_{out}	anisotropy of scattering kernel
D_{os}	λ
R	β
	screen resolution

3.2.1 ISM scattering

As described in section 2.2.2, observations of Sgr A* at sub(mm) wavelengths is subject to ISM scattering in the strong scattering regime. Due to the size of Sgr A* at mm-wavelengths, a single epoch observation of the scattering screen is further defined as falling into the *average regime*, wherein diffractive scintillation is averaged out but refractive scintillation is still present. As mm-VLBI observations can resolve the scatter-broadened image of Sgr A*, an implementation of scattering is needed which approximates the subtle changes in its extended source structure. Such an approximation has been implemented in the PYTHON-based SCATTERBRANE³ package, and is based on Johnson and Gwinn [2015]. In this algorithm a phase screen is created based on the two dimensional spatial power spectrum [see Johnson and Gwinn, 2015, Appendix C] which incorporates inner and outer turbulent lengths scales. With the screen generated, the original image is scattered according to equation 2.23. In practice equation 2.23 is implemented using an interpolation function which is modified by the values on the phase screen. SCATTERBRANE allows variation in all parameters (see table 3.2) associated with the scattering screen which is essential as aspects of the scattering towards the Galactic Centre are still unconstrained [e.g. Gwinn et al., 2014].

We include the SCATTERBRANE software, which has already yielded im-

³<http://krosenfeld.github.io/scatterbrane>

portant context for mm-VLBI observations towards Sgr A* [e.g. Ortiz-León et al., 2016], within the MEQSILHOUETTE framework. Our ISM module interfaces the SCATTERBRANE code within an interferometric simulation pipeline. This module enables simultaneous use of time-variable ISM scattering and time-variable intrinsic source structure within a single framework. The user is able to select a range of options relating to the time-resolution and epoch interpolation/averaging of both. By default, if the time resolution chosen to sample the source variability Δt_{src} and screen variability Δt_{ism} are unequal, we set

- $\Delta t_{\text{ism}} = \Delta t_{\text{src}}$ if $\Delta t_{\text{src}} < \Delta t_{\text{ism}}$
- $\Delta t_{\text{ism}} = R(\frac{\Delta t_{\text{src}}}{\Delta t_{\text{ism}}})\Delta t_{\text{src}}$ if $\Delta t_{\text{src}} > \Delta t_{\text{ism}},$

where R rounds the fraction to the nearest integer. This modification to the ISM sampling resolution avoids interpolation between different snapshots of the intrinsic source structure.

3.2.2 Atmospheric corruption simulator

Our focus in this module is to model the three primary, interrelated (see section 2.2.3) observables which are the most relevant to mm-VLBI: turbulence-driven fluctuations in the visibility phase $\delta\phi$; signal attenuation due to the atmospheric opacity τ ; and the increase in system temperature due to atmospheric emission at a brightness temperature T_{atm} due to non-zero opacity. Our approach is to model these observables as being separable into mean and turbulent components which are simulated independently [Blecher et al., 2016]. The mean tropospheric simulation module performs radiative transfer with a detailed model of the electromagnetic spectrum of each atmospheric constituent. The turbulent simulation module takes a scattering approach to account for the decoherence that results from power-law turbulence.

As described in section 2.2.3, we use the ATM package to perform radiative transfer through the realisation of the mean atmosphere. In order to calculate atmospheric temperature and pressure profiles, ATM is input several station dependent parameters, namely, ground temperature and pressure, PWV depth, water vapour scale height, tropospheric lapse rate and altitude. The lapse rate refers to the linear relation at which temperature decreases with height. Through experimentation, we have found that the first 3 variables most significantly effect the results of the simulation and opt to keep the latter variables at their default values which were set for application to ALMA. The outputs of this procedure are mean values for opacity, time delay and atmospheric brightness temperature at each station at zenith. Both opacity and time delay are separated into wet (water vapour) and dry (other) components. Furthermore, Tte time delay is subdivided into dispersive and non-dispersive components. These outputs are calculated for a list of frequencies, each representing central channel frequency. Hence, the non-dispersive component of the mean atmosphere is accounted for. We perform this calculation using representative climate conditions taken from the literature. This final step is to account for elevation effects by multiplying by the airmass $1/\sin \theta$.

Following from section 2.2.3, we derive a weak scattering formalism to calculate station dependent visibilities phase variations which result from observing through a turbulent troposphere. Specifically we simulate random walks in visibility phase with variance given by equation 2.40 for each antenna. These phase-time series are combined to form a multiplicative complex gain corruption, with amplitude of unity i.e. a diagonal Jones matrix. In section 4.1 we explore the effect of the mean and turbulent atmosphere on observables.

3.2.3 Antenna pointing error simulator

To simulate pointing errors, we use the implementation built into the MEQTREES. This functionality includes the capability to convolve station primary beams with the sky model, which is implemented as an E-Jones matrix in the RIME, see section 2.2.4. The beam models available through this function are sinc, Gaussian and the analytic WSRT beam model. The standard beam model which we will make use of is the analytic WSRT beam model [Popping and Braun, 2008]

$$E(l, m) = \cos^3(C\nu\rho), \quad \rho = \sqrt{\delta l_p^2 + \delta m_p^2} \quad (3.1)$$

where C is a constant, with value $C \approx 65 \text{ GHz}^{-1}$ for a dish diameter of 25 m. Note that the power beam EE^H becomes \cos^6 . One drawback of the MEQTREES implementation is that it is incompatible with the FITS format and so we are limited to point and Gaussian parameteric sources for the pointing error simulations. However this is not a significant issue as the pointing error should be constant across the FOV, effectively reducing to a Direction Independent Effect (DIE), and hence source structure is unimportant to pointing error analysis within the mm-VLBI framework.

Furthermore, MEQTREES allows a constant offset or time-variable primary beam, where the time variability can be either a polynomial (up to third order) or a sinusoid. We have opted to use only the sinusoidal variability for simplicity. To simulate stochastic variability i.e. pointing error due to slew between calibrator and source, we use a constant offset which is resampled per user-specified time interval. In section 4.1 we demonstrate the effect of constant, sinusoidally variable and stochastically variable pointing errors on the Large Millimeter Telescope (LMT) within the context of the EHT array.

Chapter 4

Results and analysis

In this chapter we will showcase a series of results from the MEQSILHOUETTE simulator in order to demonstrate it's capabilities and predictions.

4.1 Canonical simulations

Author's note: This section draws largely from the work of Blecher et al. [2016].

ISM variability and substructure

We remind the reader of the reproduction of the ISM-induced closure phase uncertainty result [Ortiz-León et al., 2016], shown in Fig. 2.2. To obtain this result we simulated 50 observations, each with an independent realisation of the ISM scattering screen. The success of the reproduction verifies a large section of the simulation software, including I/O, the interferometric and the ISM modules.

Following the discussion on the ISM theory (section 2.2.2), we compare predictions of the ensemble-averaging regime, which consists of only a Gaussian convolution, and the average regime, which includes the presence of

stochastic substructure. Note that the ensemble-average is invariant with time and would not bias the closure phase of a point-symmetric source.

“We present the results of a simulated observation of 10 minutes duration at 14:00 UTC on four consecutive days in Fig. 4.1. To compare to published observations, we use the three-station EHT array consisting of the Submillimeter Telescope (SMT) in Arizona, the Combined Array for Research in Millimeter-wave Astronomy (CARMA) in California and the James Clerk Maxwell Telescope (JCMT) on Mauna Kea, Hawaii. The relative transverse velocity between the observer and scattering screen is set to 50 km s^{-1} to be consistent with Ortiz-León et al. [2016]. The source is a circular Gaussian with a $\text{FHW M} = 40 \mu\text{-arcsec}$, approximately the angular distance that a scattering screen would travel over ~ 4 days. The source size has been chosen such that it is consistent with the latest estimate of the size of Sgr A* at 230 GHz [Fish et al., 2011]. Closure quantities are model dependent and calculated as specified in Rogers et al. [1995], where the thermal noise was added based on the system equivalent flux density (SEFD) table in [Lu et al., 2014].

Fig. 4.1 provides an example of closure phase and flux variability over a 4 day period using a static source. Accurate simulation of the ISM-induced closure phase variation is essential in order to make any inference on asymmetric, event-horizon scale structure [e.g. Fish et al., 2016, Ortiz-León et al., 2016]. This will become even more important as the EHT sensitivity increases by an order of magnitude in the near future when [phased ALMA is included in the array.]” [Blecher et al., 2016]

This simulation clearly shows how the longest baselines are more sensitive to the refractive substructure, which in turn strengthens the challenge of imaging compact features and/or fine structure like the BH shadow.

Recalling the variability associated with Sgr A* (section 2.1.4), if the source has intrinsic spatial variability, e.g. an orbiting hotspot model [Doeleman et al., 2009] or jet shocks, this will increase ISM variability as the relative motion between source, screen and observer is increased [Blecher et al., 2016]. Although an orbiting plasma blob might be torn apart on sub-orbit timescales by differential rotation and the non-linear shear of the Magneto-Rotational Instability [(MRI) Balbus and Hawley, 1991], this scenario becomes more of a physical possibility when resonant orbits are considered [Brink et al., 2015]. A resonant orbit occurs when the ratio of characteristic radial ω_r and longitudinal frequencies ω_θ is a rational number $\omega_r/\omega_\theta = n/m$, where $n, m \in \mathbb{N}$. A hotspot in such an orbit could be stable against differential rotation and associated shearing. In the case of Sgr A*, the 1/2 and 2/3 resonances have length scales of 41 and 55 $\mu\text{-arcsec}$ respectively for a Schwarzschild BH [Brink et al., 2015], which is observable with the EHT. Also note that these resonant length scales are greater than $r_{\text{ref}} \sim 10 \mu\text{-arcsec}$ and so the orbit would traverse independent refractive substructure fluctuations. This is relevant to methods like that demonstrated in Doeleman et al. [2009] which rely on periodic closure phases. The periodic signal would exist (albeit altered by the ISM) but only on timescales less than t_{ref} , assuming the orbiting body is unresolved.

Finally, we note that the ISM is polarisation invariant, hence the variability of polarisation ratios will not be biased by ISM scattering. Methods which use polarisation ratios [e.g. Johnson et al., 2014] allows for valuable insight into how the source variability and ISM variability could be separated.

Atmospheric transmission and scattering

As described in section 3.2.2, the implementation of the tropospheric module is separated into mean and turbulent components. For the mean atmosphere, we simulate opacity, sky brightness temperature and time delay as a function of site weather, elevation angle and frequency. The most impor-

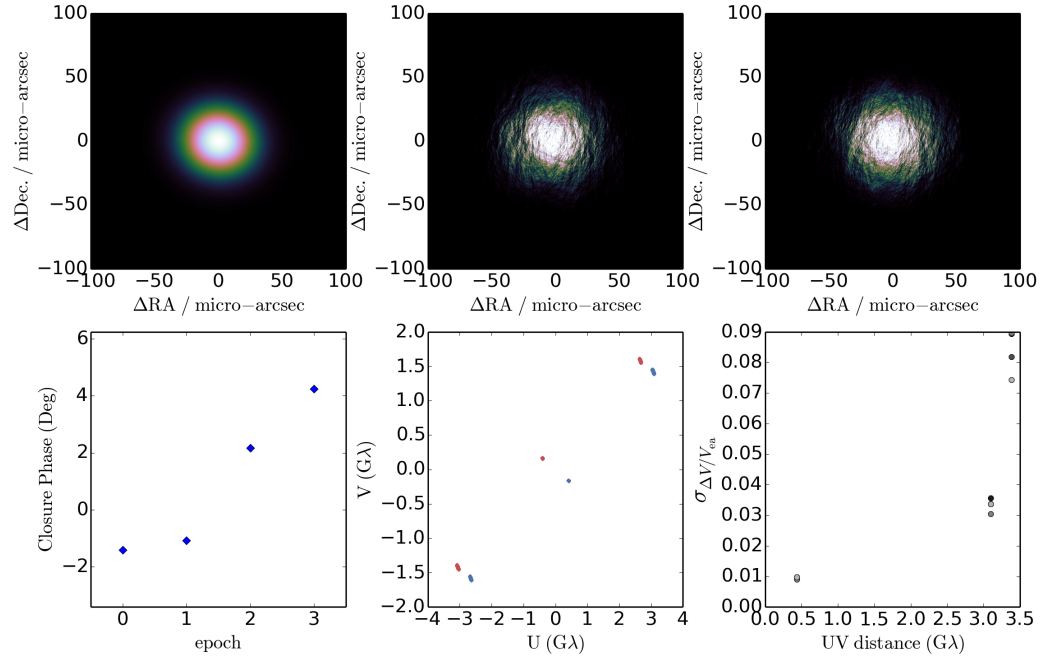


Figure 4.1: “An example simulation of ISM scattering towards Sgr A*, observed with SMT-JCMT-CARMA. The top panel, left to right, shows the original $\text{FWHM} = 40 \mu\text{-arcsec}$ Gaussian (**top left**), the simulated ISM scattered image on the first night (**top middle**) and last night (**top right**) of the observation, respectively. The bottom panel, left to right, shows the evolution of the 10 minute-averaged closure phase with epoch (**bottom left**), uv-tracks for each night (**bottom middle**) and the RMS fractional visibility amplitude differences $\sigma_{\Delta V/V_{\text{ea}}}$ as a function of uv -distance (**bottom right**). $\Delta V = (|V_a| - |V_{\text{ea}}|)$, where $|V_a|$ and $|V_{\text{ea}}|$ are the simulated average and ensemble average visibility amplitudes respectively. Variations from the ensemble-average flux on the shortest baselines reveal total flux modulation while flux variations on longer baselines and non-zero closure phases track the fluctuations in substructure.” (Image and caption reproduced from Blecher et al. [2016])

tant climate parameters are precipitable water vapour column depth (PWV), ground temperature and ground pressure. The turbulent module simulates Gaussian fluctuations in the time delay \tilde{t} arriving at each station, where $\sigma(\tilde{t})$ is based on Kolmogorov turbulence on a two-dimensional scattering screen.

The first atmospheric result we present are mean opacities and sky brightness temperatures for ALMA, the Submillimeter Array (SMA) and the South Pole Telescope (SPT) at 230 GHz, shown in Fig. 4.2. These sites were chosen as they are all considered excellent sites for sub-mm astronomy and form an essential part of the EHT. The PWV ranges used were taken from the 25th and 75th percentile data shown in Lane [1998] and is in good agreement with the measured opacities therein.

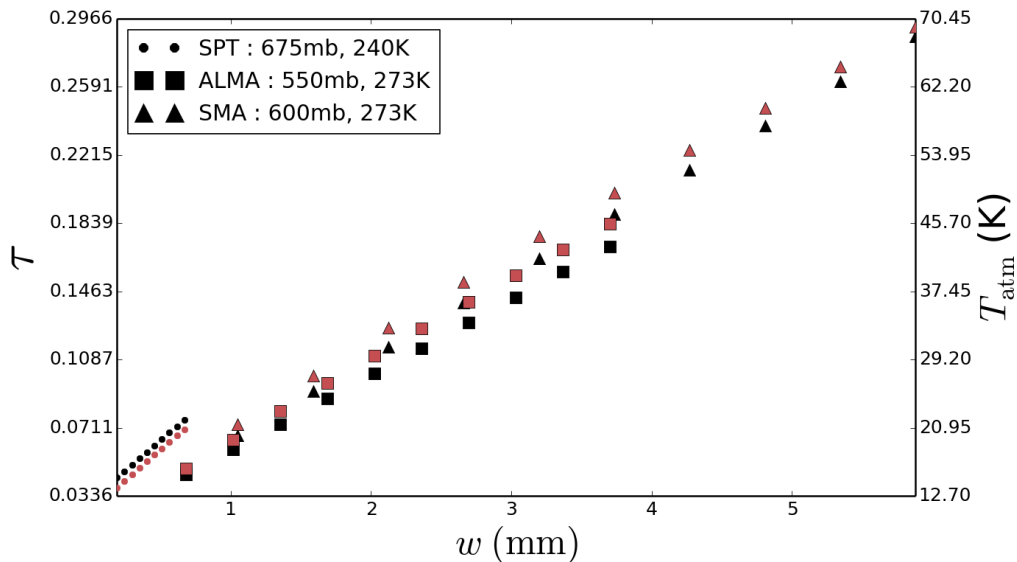


Figure 4.2: “Simulated mean opacity (black) and sky brightness temperature (red) at $\nu = 230$ GHz for three typical ground pressures and temperatures over a typical PWV range [Lane, 1998] which approximately represent the sites of SPT (dots), ALMA (squares) and SMA (triangles). The legend shows the estimated input ground (pressure, temperature) parameters for each site.” (Image and caption reproduced from Blecher et al. [2016])

Immediately apparent is that the opacity and sky brightness temperature both exhibit linear relationships with respect to PWV content. Furthermore, opacity and sky brightness temperature are proportional to ground pressure and inversely proportional to the ground temperature [Pardo et al., 2001]. It is also clear that SPT has far less opacity, and a lower sky brightness tem-

perature than ALMA and the SMA which are fairly similar. A comparison of the thermal receiver temperatures for the three sites (ALMA \sim 262 K, SMA \sim 327 K, SPT \sim 255 K) reveals that for the thermal noise contribution from the receiver is approximately an order of magnitude higher than sky brightness temperature.

Of vital importance to an interferometric site is atmospheric stability. An example of the effects of atmospheric transmission and scattering on the time delay \tilde{t} at 230 GHz is shown as a function of observation time in Fig. 4.3. Canonical values (see caption) were used for the weather parameters. It is apparent that the turbulent component is typically 3-4 orders of magnitude lower than the mean delay, even though the coherence time is on the order of seconds.

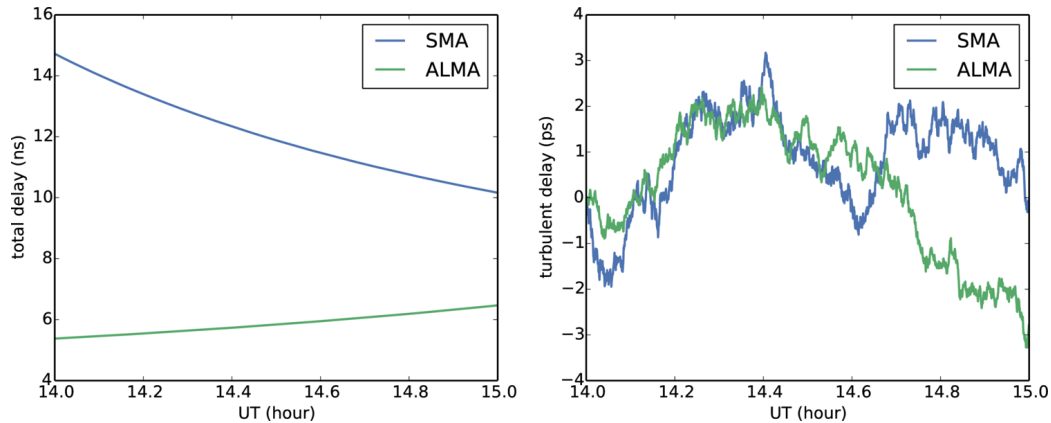


Figure 4.3: “Simulation of the total delay (left) and the turbulent atmospheric delay (right) for SMA (blue) and ALMA (green) sites towards Sgr A*. Ground pressures and temperatures are the same as Fig. 4.2, precipitable water vapour above each station is set to $w = 2$ mm, and the instantaneous zenith coherence time is set $T_0 = 10$ s for both stations. Note that all tropospheric parameters are, however, independently set. The conversion from time delay to phase at 230 GHz is 1 rad = 0.7 ps.” (Image and caption reproduced from Blecher et al. [2016])

“We now investigate the effect of the tropospheric module on

image quality for various levels of calibration accuracy. We simulate the simple scenario of a sky model that consists of a 2.4 Jy point source at the phase centre, which is an approximate EHT-measured flux density of Sgr A* at 230 GHz. We assume a zenith phase coherence time of $t_0 = 10$ s above each station (however, each stations PWV can be independently simulated). We approximate the effect of imperfect calibration by adding a small fraction of the turbulent phase noise. For this example, we do not include the mean delay component, assuming it to be perfectly corrected for during the calibration. Imaging [is performed] using the two dimensional inverse fast Fourier transform”

[Blecher et al., 2016]

Analysis of the images reveal increasing attenuation in the original peak, central flux due to the simulated residual calibration errors. In the calibration procedure, station gains cannot be solved for on arbitrarily short intervals as adequate SNR is needed to fringe-fit/self-calibrated. Aside from the fact that solutions are imperfect, within a given solution interval, there will also be a degree of uncalibrated turbulence-induced phase fluctuations.

Specifically, the flux of original central peak component is reduced to 76.5% (attenuation only - not shown in plot), 75.1% (1% turbulence), 65.5% (2% turbulence) and 40.5% (3% turbulence). In the case of 3% turbulence, the imaging artifact vertically below the source at 44.5% of the original source flux becomes brighter than the corrupted source.

Furthermore, there are slight offsets in the central peak flux from the original source position as shown by progressive movement away from the black crosshairs. This shift $\approx 5.6 \mu\text{-arcsec}$ at 3% turbulence.

The residual calibration errors also distort the interferometric artifacts (as seen in the uncorrupted image), which result from inadequate sampling of the Fourier domain before imaging. This distortion causes a breakdown in image-plane deconvolution and source finding algorithms as the Point Spread

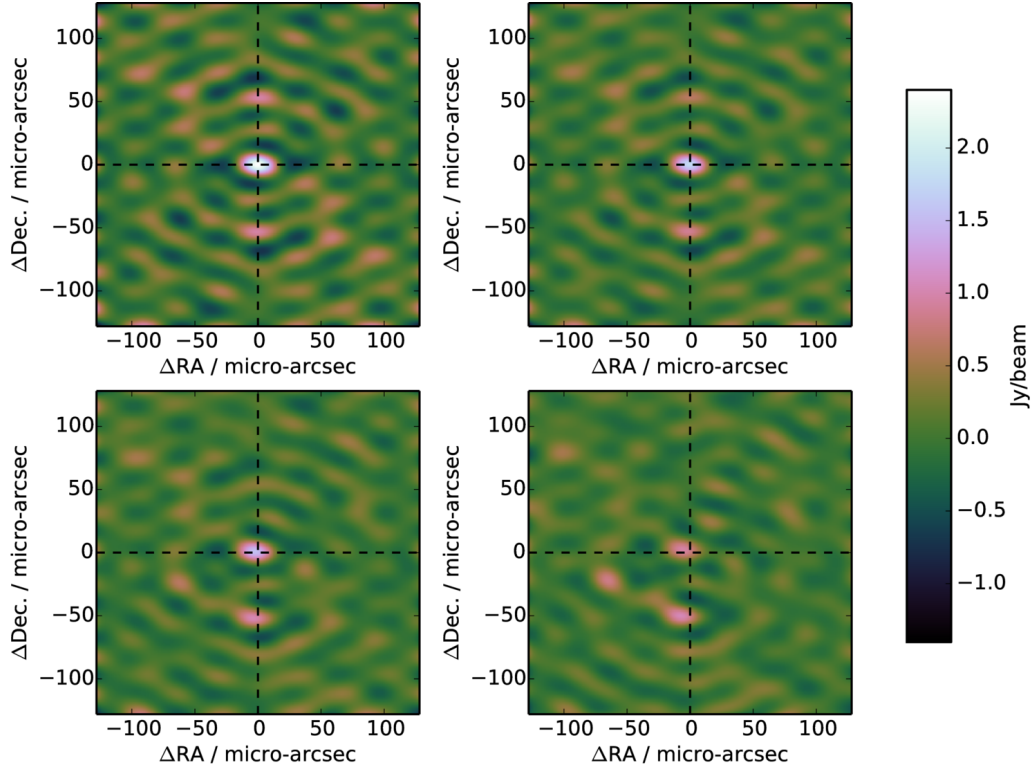


Figure 4.4: “The effect of residual troposphere phase noise on interferometric images of a point source observed for 12 hours at 230 GHz with 4 GHz bandwidth with the following array : SPT, ALMA, SMA, SMT, LMT and JCMT, assuming the same SEFDs as Lu et al. [2014] and an elevation limit of 15° . For simplicity the weather parameters at each station were set to: coherence time $t_0 = 10$ sec; PWV depth $w = 1$ mm; ground pressure $P = 600$ mb; ground temperature $T = 273$ K. **Top left:** interferometric map with thermal noise only. **Top right:** atmospheric attenuation and sky noise (due to non-zero opacity) with 1% of the turbulent phase noise added. **Bottom left:** as previous but with 3% of turbulent phase contribution. **Bottom right:** as previous but with 6% turbulent phase contribution. The fractional turbulent phase contributions are illustrative of the effect of fringe-fitting errors. The black crosshairs indicate the original source position. ”(Image and caption reproduced from Blecher et al. [2016])

Function (PSF) is difficult to subtract and the interferometric artefacts are difficult to distinguish from source structure. This further weakens the ability of such source finding algorithms to extract, with high fidelity, the BH shadow feature.

There was no evidence of blurring or a loss of resolution in the simulated images of Fig. 4.4. Blurring can result if the decoherence is considered proportional to baseline length, as longer baselines would be less coherent and so their visibility amplitudes are effectively downweighted. For the EHT, as different stations experience completely independent phase fluctuations, the baseline length of the VLBI baselines will not be correlated with the magnitude of the decoherence. Alternatively, the blurring consequence, characteristic in optical single dish telescopes as 'seeing', is induced by the overlaying of many speckled images of the source [Narayan, 1992] across the scattering disc. This does not seem to occur in the interferometric image reconstruction with the inverse fourier transform. The reason being that the phase noise of each fourier mode is Gaussian, and so positional deviations of each Fourier mode from zero phase noise effectively cancel in the image domain. Hence attenuation but no blurring.

Antenna pointing offset

"We investigate the effect of pointing errors on the 50 m (i.e. fully illuminated) Large Millimeter Array (LMT) dish configured in an eight station VLBI array. The LMT has been measured to have an absolute pointing accuracy of $\sigma_{\text{abs}} = 1 - 3$ arcsec, where smaller offsets occur when observing sources closer to zenith, and a tracking pointing accuracy $\sigma_{\text{track}} < 1$ arcsec¹. We investigate the observational effect of these errors through three different pointing error models which explore different instructive and plausible scenarios. The LMT has been singled out due to

¹<http://www.lmtgtm.org/telescope/telescope-description/>

its narrow primary beam and that it may serve as a reference station for the EHT array given its sensitivity and central geographic location.

The source used is a circular Gaussian of characteristic size $\Theta_{\text{src}} = 50 \mu\text{-arcsec}$, located at the phase centre. For this investigation, as long as $\Theta_{\text{src}} \ll \theta_{\text{PB}}$, the exact structure of the source is unimportant. We approximate the LMT beam profile using an analytic WSRT beam model (equation 3.1) with a factor of two increase in the beam factor C to take into account the increased dish size of the LMT. [Hence] $C_{\text{LMT}} \approx 130 \text{ GHz}^{-1}$. Note that the power beam EE^H becomes \cos^6 , resulting in a FWHM = 6.5 arcsec at 230 GHz.

We make use of the RMS fractional visibility amplitude error $\sigma_{\Delta V/V_0}$, where V_{PE} and V_0 are the visibility amplitudes with and without pointing errors respectively, and $\Delta V = V_{\text{PE}} - V_0$.

[Blecher et al., 2016]

For this simulation we use three different pointing error models, as introduced in section 2.2.4. Firstly, we simulate a simple *constant* pointing offset. For the second case, we simulate a smooth, *sinusoidal* pointing error to replicate a tracking error. The period of the sinusoid is sampled from a uniform distribution between 0.5 and 6 hours, and a peak amplitude $A_\rho = \sqrt{2}\sigma_\rho$, where the factor $\sqrt{2}$ relates the peak amplitude to the RMS of a sinusoidal, zero-mean waveform. In the third case, we simulate *stochastic* variability which replicates slewing from source/calibrator to source/calibrator, where the pointing error is re-sampled every 10 minutes from a Gaussian of characteristic width equal to the quoted pointing error. This simulation is repeated for 50 realisations for each pointing offset to generate reasonable uncertainties [Blecher et al., 2016]. In Fig. 4.5, $\sigma_{\Delta V/V_0}$ is plotted against pointing error ρ over the range $0 \leq \rho \leq 4.5$ arcsec for the three classes of error. Note that although plotted on the same set of axes, ρ represents slightly different

quantities for each of the three simulations.

“We only consider LMT pointing errors due to its narrow primary beam and potential to be used as a reference station. However, the capability to simulate independent pointing errors for each station is available. In the case of a phased array, a pointing error simulation could be used to investigate the contribution of the pointing error to a variable phasing efficiency, which can be reasonably approximated by a scalar Jones matrix.”

[Blecher et al., 2016]

“Visibility amplitude errors due to antenna pointing error has been investigated for the 50 m LMT dish operating at 230 GHz. In Fig. 4.5, we show that pointing errors associated with frequent phase centre switching (stochastic variability) could introduce a RMS fractional amplitude error $\sigma_{\Delta V/V_0} \sim 0.1 - 0.4$ for an absolute pointing accuracy $\sigma_{\text{abs}} \sim 1 - 3$ arcsec. In contrast, tracking errors are less problematic with $\sigma_{\Delta V/V_0} \leq 0.05$ for a tracking accuracy $\sigma_{\text{track}} < 1$ arcsec. The case of a constant error pointing model is comparable to that of the ‘slow variability’ case. If the gain error is non-separable from the calibration model used, it could be interpreted as intrinsic variability, substructure and/or increased noise. If unaccounted for, this effect has the potential to limit the dynamic range of mm-VLBI images. Further tests to constrain the pointing uncertainties of EHT stations will lead to more accurate interferometric simulations and hence the overall impact on black hole shadow parameter estimation. Here we demonstrate the capability to incorporate a range of plausible pointing error effects into a full simulation pipeline. For future observations at 345 GHz, these effects will be even more pronounced, given the

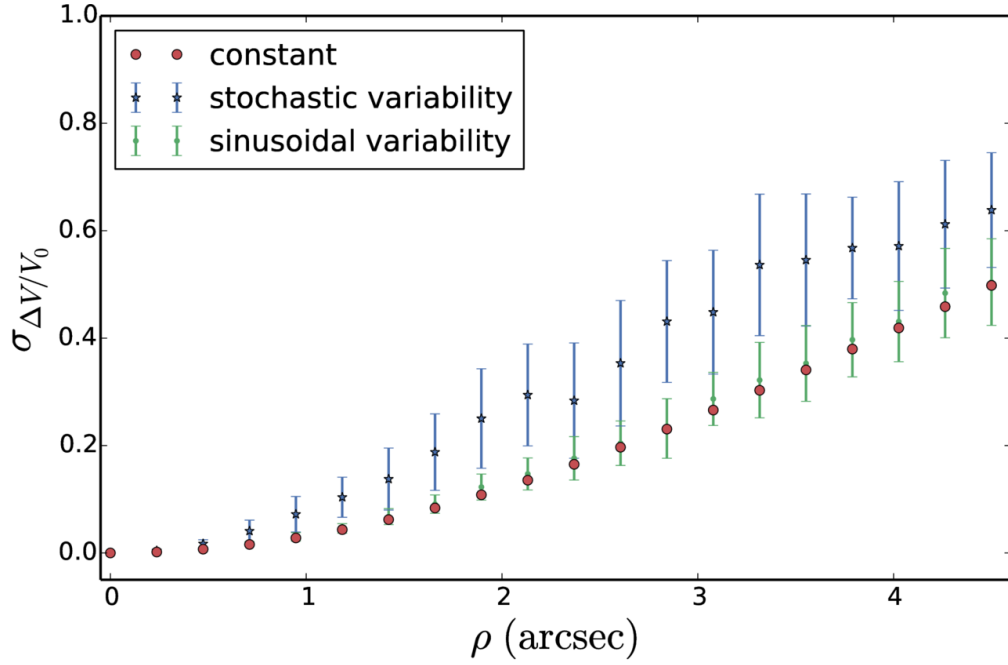


Figure 4.5: “RMS relative amplitude error induced by pointing error with the 50 m (i.e. fully illuminated) LMT antenna as a function of pointing error offset ρ at 230 GHz. We assume that these errors are degenerate or non-separable from the self-calibration/fringe-fitting model used. See text for the description of the three models used. This simulation capability enables constraints on the magnitude of pointing-induced errors given a particular pointing calibration strategy.” (Image and caption reproduced from Blecher et al. [2016])

narrower primary beam.

[Blecher et al., 2016]

4.2 Suggested applications and improvements

Anomalous pointing error

There is another class of pointing error which we did not include in our simulation, but which should be folded in through a combination of the tro-

pospheric and antenna pointing modules. This effect is called the ‘anomalous refraction’ and is due to the time-variable phase-gradient across the aperture [e.g. Holdaway, 1997, Butler, 1997, Holdaway and Woody, 1998]. This is essentially the first order fluctuation in water vapour across the dish diameter d_{dish} (i.e. a wedge) and hence will be a function of $D_\phi(d_{\text{dish}})$. These are pointing errors which will change on the timescale $d_{\text{dish}}/v \sim 1 - 50$ s for $10 < d_{\text{dish}} < 50$ m and $1 < v < 10$ m/s, where d_{dish} is the diameter of the aperture.

Holdaway and Woody [1998] derive the standard deviation of the pointing error as a fraction of beam width,

$$\sigma_{\text{pe}}(d_{\text{dish}}), \theta = \frac{\sqrt{2D_l(d_{\text{dish}})}}{\sqrt{\sin \theta} \lambda}, \quad (4.1)$$

where l is the extra electric path length and θ is the elevation angle. Hence in terms of fractional beam size, the effect goes as $d_{\text{dish}}^{\beta/2}$ and hence the effect for large dishes will be larger amplitude variations (as shown by Fig. 4.5) over longer time periods.

Apertures which are fitted with water vapour radiometers are able to track the PWV distribution across the primary beam [Lamb and Woody, 1998]. However, most of the EHT stations are currently not fitted with radiometers and hence this effect could be tricky to calibrate.

Testing calibration, imaging and parameter estimation

The primary use of synthetic data is to provide ‘known’ datasets on which to run calibration, imaging and parameter estimation pipelines. This can take the form of beauty contests, where various algorithms are utilised without knowledge of the true source and the results are compared post-facto. This is especially useful with imaging algorithms which have many ‘hand-tuned’ parameters and difficulty with repeatability, uniqueness and fidelity of their solutions. Alternatively, one could perform a more systematic investigation

of how an algorithm performs under a range different conditions. A key test which we have alluded to throughout this thesis is a systematic exploration of the turbulent tropospheric effects on the accuracy of fringe-fitting algorithms/strategies, including the added complexity of a time-variable source. A key point of such an investigation being the capability of assigning quantitative values to systematic and stochastic uncertainties across a wide range of physically relevant conditions.

With the current work developing automated fringe-fitters at JIVE (casa-based) and UCT/SKA-SA (bayesian) by Des Small and Iniyan Natarajan respectively, there arises the possibility of an end-to-end simulation pipeline, i.e. from theory to calibrated data product, within the next year. In this scenario, one could estimate the precision and accuracy with which the EHT could extract parameters (e.g. shadow size and asymmetry) in a range of canonical scenarios. This will also allow weak points in the calibration/analysis to be identified and subsequently improved as well as to determine which approaches to extracting science are more viable (e.g. analysis in the visibility domain vs image domain). This argument can be extended to the realm of station upgrades (e.g. enhanced bandwidth) and the investigation into novel (sub)millimetre sites.

As the EHT will be observing in a unique regime, there will always be doubt, double-checking and questioning of the interpretation of the data. This is especially the case with the use of closure quantities, where the recent result of an increase in closure phase with UT hour, measured on the Hawaii-Arizona-California triangle [Fish et al., 2016], provides a good example. Simulations help formulate and test quantitatively plausible scenarios. For example the contribution of different components (e.g. ISM substructure, SNR) to the scatter in this result could be investigated for different source models.

“Significant progress has been made in the theoretical and numerical modeling of the inner accretion flow and jet launch

regions near a supermassive black hole event horizon [e.g. Del Zanna et al., 2007, Etienne et al., 2010, Dexter and Fragile, 2013, Mościbrodzka et al., 2014, McKinney et al., 2014]. As the sensitivity of the EHT stands to dramatically increase, these theoretical efforts must be complemented by advances in interferometric simulations. With MEQSILHOUETTE, we now have the ability to couple these with sophisticated interferometric and signal propagation simulations. Moreover, detailed interferometric simulations will enable us to quantify systematic effects on the black hole and/or accretion flow parameter estimation.”

[Blecher et al., 2016]

A public online interface

Table 3.1 shows the set of parameters needed to run a standard MEQSILHOUETTE simulation. This moderate number of parameters ($24 + 6N_{\text{stations}}$) can be quickly chosen or selected from a list, especially if most of the defaults are preset and unlikely to change. This speaks to the possibility of an online GUI interface which would provide the user with the capability to run standard simulations without having to delve into code. The capability to run such simulations would be useful to both theorists and observers in the broader AGN/SMBH/mm-VLBI community. For this reason, we trialed an online interface at the Leiden 2015 mm-VLBI workshop² with an early version of the MEQSILHOUETTE simulator, which was well received by the researchers present. We are, however, yet to convert the latest version of the pipeline [Blecher et al., 2016] into such an interface, but hopefully this implementation will be made available in the future when matters relating to public/propriety status of the codebase are cleared up.

²<http://www.astron.nl/other/workshop/mm-VLBI2015>

Full Stokes

One of the key observables for the EHT is polarisation dependent quantities [Johnson et al., 2015]. Although this version focused only on total intensity, if MEQSILHOUETTE is taken up by members of the community, subsequent versions will enable the full Stokes cube as input. This should not entail much work as our chosen data formats (MS, FITS) as well as the FFT and UV sampling routine in MEQTREES already support full Stokes logic including parallactic angle rotation. Signal propagation through the ISM and troposphere as well as antenna based complex gains errors are polarisation independent. The work would be primarily involve altering the existing scripts to deal with the book-keeping of the extra dimension. In addition the implementation of the associated signal corruption, polarisation leakage, is straightforward in the RIME formalism as it is simply an off-diagonal Jones matrix which is approximately constant over the course of an observation.

Chapter 5

Conclusion

In light of upcoming EHT observations and science goals as well as software advances in the broader radio interferometry community, a mm-VLBI data simulator has been developed as described first in Blecher et al. [2016] and expanded upon in this thesis.

We believe that our design objectives, laid out in section 3.1, is apparent from the diversity of simulations shown by our results. This work provides the first evidence that an end-to-end simulator is possible for the EHT and outlines the design and utilities from its construction. Even though the foundation of the simulator has been built, it is only through collaboration with the various EHT working groups that its potential will truly be achieved.

The focus has been placed on simulating realistic data given an arbitrary theoretical sky model. The pipeline uses the MEASUREMENT SET format, in line with ALMA and future VLBI data formats, however as there are various other data formats currently in use, collaboration will require reliable conversion.

We have placed focus has been placed on EHT observations, however, the pipeline is completely general with respect to observation configuration and allow any source structure in the form of FITS format. Time variability in all domains (source, array, ISM, troposphere) is implemented. We highlight this

point as we view the development of calibration and imaging routines which deal appropriately with source variability an essential challenge for observations of Sgr A*. Distinguishing complex gain variations, i.e. \mathbf{G} -Jones terms from short intrinsic variability will depend on the SNR obtained, where the inclusion of ALMA in the array will be pivotal in this regard. However, software advances can also add further utility. A synthetic data simulator could prove essential to research and test calibration, imaging and parameter estimation strategies. To this end, the simulator includes signal corruptions in the interstellar medium (ISM), troposphere and instrumentation. Examples of typical corruptions have been demonstrated, which show that each corruption can significantly affect the inferred scientific parameters. A wide range of signal propagation effects can be implemented using the Measurement Equation formalism, and the simulator can be easily extended to include bandpass imperfections and polarisation leakage.

The ISM scattering implementation SCATTERBRANE, based on Johnson and Gwinn [2015], has been incorporated into the pipeline. We have discussed how ISM substructure and variability can be difficult to disentangle from the intrinsic source structure, especially if the source is also variable. The magnitude of the refractive substructure will depend on the size of the emission region which at 1.3mm is sensitive to optical depth effects due to synchrotron self-absorption and accretion history. If possible, observations of Sgr A* should ideally be spaced apart by $r_{\text{ref}}/v \sim$ a week in order to sample independent realisations of the scattering screen.

Where we simulated images of a point sources with residual calibration errors, we find rapidly increasing flux attenuation from 1% at 1% turbulence to 36% at 3% turbulence. We also find offsets of a few microarcseconds. Interestingly the remnants of the PSF in the image are also distorted which can cause them to be difficult to identify as artefacts of the imaging procedure.

We have simulated the effects of antenna pointing error models corresponding to tracking or slew errors on the LMT. Furthermore, we have briefly

discussed the effects of the turbulent atmosphere on antenna pointing. This ‘anomalous’ pointing error is potentially a serious calibration difficulty for sites without radiometers.

Applications for which the current version of the pipeline is well suited for include testing calibration and imaging routines in total intensity. One example which we have discussed is fringe-fitting in the presence of a variable troposphere with time-variable source. The creation of a close interface between sophisticated theoretical and interferometric mm-VLBI simulations will enhance the scientific opportunities possible with the EHT.

If the development of MEQSILHOUETTE is continued, future capabilities would include a full Stokes capability including polarised sources and polarisation leakage as well as the simulation of pointing errors due to ‘anomalous refraction’. To promote connection between theory and data, a standard version of MEQSILHOUETTE could be run through an online interface. This would make interferometric simulations public or available to the mm-VLBI community.

Bibliography

- J. W. Armstrong, B. J. Rickett, and S. R. Spangler. Electron density power spectrum in the local interstellar medium. *ApJ*, 443:209, apr 1995. doi: 10.1086/175515. URL <http://dx.doi.org/10.1086/175515>.
- D. C. Backer. Scattering of radio emission from the compact object in Sagittarius A. *ApJ*, 222:L9–L12, May 1978. doi: 10.1086/182681.
- F. K. Baganoff, M. W. Bautz, W. N. Brandt, G. Chartas, E. D. Feigelson, G. P. Garmire, Y. Maeda, M. Morris, G. R. Ricker, L. K. Townsley, and F. Walter. Rapid X-ray flaring from the direction of the supermassive black hole at the Galactic Centre. *Nature*, 413:45–48, September 2001. doi: 10.1038/35092510.
- S. A. Balbus and J. F. Hawley. A powerful local shear instability in weakly magnetized disks. I - Linear analysis. II - Nonlinear evolution. *ApJ*, 376: 214–233, July 1991. doi: 10.1086/170270.
- S. A. Balbus and J. F. Hawley. Instability, turbulence, and enhanced transport in accretion disks. *Reviews of Modern Physics*, 70:1–53, January 1998. doi: 10.1103/RevModPhys.70.1.
- G. Bélanger, R. Terrier, O. C. de Jager, A. Goldwurm, and F. Melia. Periodic Modulations in an X-ray Flare from Sagittarius A*. *Journal of Physics Conference Series*, 54:420–426, December 2006. doi: 10.1088/1742-6596/54/1/066.

T. Blecher, R. Deane, G. Bernardi, and O. Smirnov. MeqSilhouette : A mm-VLBI observation and signal corruption simulator. *MNRAS*, September 2016. doi: 10.1093/mnras/stw2311.

Max Born and Emil Wolf. Principles of optics. *Pergamon, New York*, 1980.

K. L. Bouman, M. D. Johnson, D. Zoran, V. L. Fish, S. S. Doeleman, and W. T. Freeman. Computational Imaging for VLBI Image Reconstruction. *ArXiv e-prints*, dec 2015.

G. C. Bower, H. Falcke, R. M. Herrnstein, J.-H. Zhao, W. M. Goss, and D. C. Backer. Detection of the Intrinsic Size of Sagittarius A* Through Closure Amplitude Imaging. *Science*, 304:704–708, April 2004. doi: 10.1126/science.1094023.

Geoffrey C. Bower, W. M. Goss, Heino Falcke, Donald C. Backer, and Yoram Lithwick. The Intrinsic Size of Sagittarius A* from 0.35 to 6 cm. *ApJ*, 648(2):L127–L130, aug 2006. doi: 10.1086/508019. URL <http://dx.doi.org/10.1086/508019>.

Geoffrey C Bower, Adam Deller, Paul Demorest, Andreas Brunthaler, Ralph Eatough, Heino Falcke, Michael Kramer, KJ Lee, and Laura Spitler. The angular broadening of the galactic center pulsar sgr j1745-29: A new constraint on the scattering medium. *ApJ*, 780(1):L2, 2013.

J. Brink, M. Geyer, and T. Hinderer. Astrophysics of resonant orbits in the Kerr metric. *Phys. Rev. D*, 91(8):083001, April 2015. doi: 10.1103/PhysRevD.91.083001.

A. E. Broderick, V. L. Fish, S. S. Doeleman, and A. Loeb. Constraining the Structure of Sagittarius A*'s Accretion Flow with Millimeter Very Long Baseline Interferometry Closure Phases. *ApJ*, 738:38, September 2011. doi: 10.1088/0004-637X/738/1/38.

Avery E. Broderick and Abraham Loeb. IMAGING THE BLACK HOLE SILHOUETTE OF M87: IMPLICATIONS FOR JET FORMATION AND BLACK HOLE SPIN. *ApJ*, 697(2):1164–1179, may 2009. doi: 10.1088/0004-637x/697/2/1164. URL <http://dx.doi.org/10.1088/0004-637x/697/2/1164>.

Avery E. Broderick, Tim Johannsen, Abraham Loeb, and Dimitrios Psaltis. TESTING THE NO-HAIR THEOREM WITH EVENT HORIZON TELESCOPE OBSERVATIONS OF SAGITTARIUS A*. *ApJ*, 784(1):7, feb 2014. doi: 10.1088/0004-637x/784/1/7. URL <http://dx.doi.org/10.1088/0004-637x/784/1/7>.

Avery E. Broderick, Vincent L. Fish, Michael D. Johnson, Katherine Rosenfeld, Carlos Wang, Sheperd S. Doeelman, Kazunori Akiyama, Tim Johannsen, and Alan L. Roy. MODELING SEVEN YEARS OF EVENT HORIZON TELESCOPE OBSERVATIONS WITH RADIATIVELY INEFFICIENT ACCRETION FLOW MODELS. *ApJ*, 820(2):137, mar 2016. doi: 10.3847/0004-637x/820/2/137. URL <http://dx.doi.org/10.3847/0004-637x/820/2/137>.

Brian Butler. Another look at anomalous refraction on chajnantor. 1997.

C. L. Carilli and M. A. Holdaway. Tropospheric phase calibration in millimeter interferometry. *Radio Science*, 34(4):817–840, jul 1999. doi: 10.1029/1999rs900048. URL <http://dx.doi.org/10.1029/1999rs900048>.

CL Carilli and MA Holdaway. Application of Fast Switching Phase Calibration at mm Wavelengths on 33 km Baselines. *MMA/ALMA Memorandum Series No 173, NRAO*, 1997.

A. A. Chael, M. D. Johnson, R. Narayan, S. S. Doeelman, J. F. C. Wardle, and K. L. Bouman. High-resolution Linear Polarimetric Imaging for the Event Horizon Telescope. *ApJ*, 829:11, September 2016. doi: 10.3847/0004-637X/829/1/11.

- C. E. Coulman. Fundamental and Applied Aspects of Astronomical “Seeing”. *Annual Review of Astronomy and Astrophysics*, 23(1):19–57, sep 1985. doi: 10.1146/annurev.aa.23.090185.000315. URL <http://dx.doi.org/10.1146/annurev.aa.23.090185.000315>.
- Emily I Curtis, Bojan Nikolic, John S Richer, and Juan R Pardo. Atmospheric dispersion and the implications for phase calibration. *arXiv preprint arXiv:0912.2852*, 2009.
- L. Del Zanna, O. Zanotti, N. Bucciantini, and P. Londrillo. ECHO: a Eulerian conservative high-order scheme for general relativistic magnetohydrodynamics and magnetodynamics. *A&A*, 473:11–30, October 2007. doi: 10.1051/0004-6361:20077093.
- J. Dexter and P. C. Fragile. Tilted black hole accretion disc models of Sagittarius A*: time-variable millimetre to near-infrared emission. *MNRAS*, 432:2252–2272, July 2013. doi: 10.1093/mnras/stt583.
- S. Doeleman, E. Agol, D. Backer, F. Baganoff, G. C. Bower, A. Broderick, A. Fabian, V. Fish, C. Gammie, P. Ho, M. Honman, T. Krichbaum, A. Loeb, D. Marrone, M. Reid, A. Rogers, I. Shapiro, P. Strittmatter, R. Tilanus, J. Weintraub, A. Whitney, M. Wright, and L. Ziurys. Imaging an Event Horizon: submm-VLBI of a Super Massive Black Hole. In *astro2010: The Astronomy and Astrophysics Decadal Survey*, volume 2010 of *Astronomy*, 2010.
- S. S. Doeleman, Z.-Q. Shen, A. E. E. Rogers, G. C. Bower, M. C. H. Wright, J. H. Zhao, D. C. Backer, J. W. Crowley, R. W. Freund, P. T. P. Ho, K. Y. Lo, and D. P. Woody. Structure of Sagittarius A* at 86 GH[CLC]z[/CLC] using VLBI Closure Quantities. *AJ*, 121(5):2610–2617, may 2001. doi: 10.1086/320376. URL <http://dx.doi.org/10.1086/320376>.
- Sheperd S. Doeleman, Jonathan Weintraub, Alan E. E. Rogers, Richard Plambeck, Robert Freund, Remo P. J. Tilanus, Per Friberg, Lucy M. Zi-

- urys, James M. Moran, Brian Corey, Ken H. Young, Daniel L. Smythe, Michael Titus, Daniel P. Marrone, Roger J. Cappallo, Douglas C.-J. Bock, Geoffrey C. Bower, Richard Chamberlin, Gary R. Davis, Thomas P. Krichbaum, James Lamb, Holly Maness, Arthur E. Niell, Alan Roy, Peter Strittmatter, Daniel Werthimer, Alan R. Whitney, and David Woody. Event-horizon-scale structure in the supermassive black hole candidate at the Galactic Centre. *Nature*, 455(7209):78–80, sep 2008. doi: 10.1038/nature07245. URL <http://dx.doi.org/10.1038/nature07245>.
- Sheperd S. Doeleman, Vincent L. Fish, Avery E. Broderick, Abraham Loeb, and Alan E. E. Rogers. DETECTING FLARING STRUCTURES IN SAGITTARIUS A* WITH HIGH-FREQUENCY VLBI. *ApJ*, 695(1):59–74, mar 2009. doi: 10.1088/0004-637x/695/1/59. URL <http://dx.doi.org/10.1088/0004-637x/695/1/59>.
- Z. B. Etienne, Y. T. Liu, and S. L. Shapiro. Relativistic magnetohydrodynamics in dynamical spacetimes: A new adaptive mesh refinement implementation. *Phys. Rev. D*, 82(8):084031, October 2010. doi: 10.1103/PhysRevD.82.084031.
- H Falcke and S B Markoff. Toward the event horizon—the supermassive black hole in the Galactic Center. *Class. Quantum Grav.*, 30(24):244003, nov 2013. doi: 10.1088/0264-9381/30/24/244003. URL <http://dx.doi.org/10.1088/0264-9381/30/24/244003>.
- Heino Falcke, W. M. Goss, Hiroshi Matsuo, Peter Teuben, Jun-Hui Zhao, and Robert Zylka. The Simultaneous Spectrum of Sagittarius A* from 20 Centimeters to 1 Millimeter and the Nature of the Millimeter Excess. *ApJ*, 499(2):731–734, jun 1998. doi: 10.1086/305687. URL <http://dx.doi.org/10.1086/305687>.
- V. L. Fish, S. S. Doeleman, A. E. Broderick, A. Loeb, and A. E. E. Rogers. Detecting Changing Polarization Structures in Sagittarius A* with High

Frequency VLBI. *ApJ*, 706:1353–1363, December 2009. doi: 10.1088/0004-637X/706/2/1353.

Vincent L. Fish, Sheperd S. Doebleman, Christopher Beaudoin, Ray Blundell, David E. Bolin, Geoffrey C. Bower, Richard Chamberlin, Robert Freund, Per Friberg, Mark A. Gurwell, Mareki Honma, Makoto Inoue, Thomas P. Krichbaum, James Lamb, Daniel P. Marrone, James M. Moran, Tomoaki Oyama, Richard Plambeck, Rurik Primiani, Alan E. E. Rogers, Daniel L. Smythe, Jason SooHoo, Peter Strittmatter, Remo P. J. Tilanus, Michael Titus, Jonathan Weintroub, Melvyn Wright, David Woody, Ken H. Young, and Lucy M. Ziurys. 1.3 mm WAVELENGTH VLBI OF SAGITTARIUS A*: DETECTION OF TIME-VARIABLE EMISSION ON EVENT HORIZON SCALES. *ApJ*, 727(2):L36, jan 2011. doi: 10.1088/2041-8205/727/2/l36. URL <http://dx.doi.org/10.1088/2041-8205/727/2/136>.

Vincent L. Fish, Michael D. Johnson, Ru-Sen Lu, Sheperd S. Doebleman, Katherine L. Bouman, Daniel Zoran, William T. Freeman, Dimitrios Psaltis, Ramesh Narayan, Victor Pankratius, Avery E. Broderick, Carl R. Gwinn, and Laura E. Vertatschitsch. IMAGING AN EVENT HORIZON: MITIGATION OF SCATTERING TOWARD SAGITTARIUS A*. *ApJ*, 795(2):134, oct 2014. doi: 10.1088/0004-637x/795/2/134. URL <http://dx.doi.org/10.1088/0004-637x/795/2/134>.

Vincent L. Fish, Michael D. Johnson, Sheperd S. Doebleman, Avery E. Broderick, Dimitrios Psaltis, Ru-Sen Lu, Kazunori Akiyama, Walter Alef, Juan Carlos Algaba, Keiichi Asada, Christopher Beaudoin, Alessandra Bertarini, Lindy Blackburn, Ray Blundell, Geoffrey C. Bower, Christiaan Brinkerink, Roger Cappallo, Andrew A. Chael, Richard Chamberlin, Chi-Kwan Chan, Geoffrey B. Crew, Jason Dexter, Matt Dexter, Sergio A. Dzib, Heino Falcke, Robert Freund, Per Friberg, Christopher H. Greer, Mark A. Gurwell, Paul T. P. Ho, Mareki Honma, Makoto Inoue, Tim Johannsen, Junhan Kim, Thomas P. Krichbaum, James Lamb,

- Jonathan León-Tavares, Abraham Loeb, Laurent Loinard, David MacMahon, Daniel P. Marrone, James M. Moran, Monika Mościbrodzka, Gisela N. Ortiz-León, Tomoaki Oyama, Feryal Özel, Richard L. Plambeck, Nicolas Pradel, Rurik A. Primiani, Alan E. E. Rogers, Katherine Rosenfeld, Helge Rottmann, Alan L. Roy, Chester Ruszczyk, Daniel L. Smythe, Jason SooHoo, Justin Spilker, Jordan Stone, Peter Strittmatter, Remo P. J. Tilanus, Michael Titus, Laura Vertatschitsch, Jan Wagner, John F. C. Wardle, Jonathan Weintraub, David Woody, Melvyn Wright, Paul Yamaguchi, André Young, Ken H. Young, J. Anton Zensus, and Lucy M. Ziurys. PERSISTENT ASYMMETRIC STRUCTURE OF SAGITTARIUS A* ON EVENT HORIZON SCALES. *ApJ*, 820(2):90, mar 2016. doi: 10.3847/0004-637x/820/2/90. URL <http://dx.doi.org/10.3847/0004-637x/820/2/90>.
- C. F. Gammie, J. C. McKinney, and G. Tóth. HARM: A Numerical Scheme for General Relativistic Magnetohydrodynamics. *ApJ*, 589:444–457, May 2003. doi: 10.1086/374594.
- K. Gebhardt, R. Bender, G. Bower, A. Dressler, S. M. Faber, A. V. Filippenko, R. Green, C. Grillmair, L. C. Ho, J. Kormendy, T. R. Lauer, J. Magorrian, J. Pinkney, D. Richstone, and S. Tremaine. A Relationship between Nuclear Black Hole Mass and Galaxy Velocity Dispersion. *ApJ*, 539:L13–L16, August 2000. doi: 10.1086/312840.
- R. Genzel, R. Schödel, T. Ott, A. Eckart, T. Alexander, F. Lacombe, D. Rouan, and B. Aschenbach. Near-infrared flares from accreting gas around the supermassive black hole at the Galactic Centre. *Nature*, 425: 934–937, October 2003. doi: 10.1038/nature02065.
- S. Gillessen, F. Eisenhauer, T. K. Fritz, H. Bartko, K. Dodds-Eden, O. Pfuhl, T. Ott, and R. Genzel. The Orbit of the Star S2 Around SGR A* from Very Large Telescope and Keck Data. *ApJ*, 707:L114–L117, December 2009. doi: 10.1088/0004-637X/707/2/L114.

- C. Goddi, H. Falcke, M. Kramer, L. Rezzolla, C. Brinkerink, T. Bronzwaer, R. Deane, M. De Laurentis, G. Desvignes, J. R. J. Davelaar, F. Eisenhauer, R. Eatough, R. Fraga-Encinas, C. M. Fromm, S. Gillessen, A. Grenzebach, S. Issaoun, M. Janßen, R. Konoplya, T. P. Krichbaum, R. Laing, K. Liu, R.-S. Lu, Y. Mizuno, M. Moscibrodzka, C. Müller, H. Olivares, O. Porth, O. Pfuhl, E. Ros, F. Roelofs, K. Schuster, R. Tilanus, P. Torne, I. van Bemmel, H. J. van Langevelde, N. Wex, Z. Younsi, and A. Zhidenko. BlackHoleCam: fundamental physics of the Galactic center. *ArXiv e-prints*, June 2016.
- J. Goodman and R. Narayan. The shape of a scatter-broadened image - II. Interferometric visibilities. *MNRAS*, 238(3):995–1028, jun 1989. doi: 10.1093/mnras/238.3.995. URL <http://dx.doi.org/10.1093/mnras/238.3.995>.
- C. R. Gwinn, M. D. Johnson, J. E. Reynolds, D. L. Jauncey, A. K. Tzioumis, H. Hirabayashi, H. Kobayashi, Y. Murata, P. G. Edwards, S. Dougherty, B. Carlson, D. del Rizzo, J. F. H. Quick, C. S. Flanagan, and P. M. McCulloch. Size of the Vela Pulsar’s Emission Region at 18 cm Wavelength. *ApJ*, 758:7, October 2012. doi: 10.1088/0004-637X/758/1/7.
- C. R. Gwinn, Y. Y. Kovalev, M. D. Johnson, and V. A. Soglasnov. DISCOVERY OF SUBSTRUCTURE IN THE SCATTER-BROADENED IMAGE OF SGR A*. *ApJ*, 794(1):L14, sep 2014. doi: 10.1088/2041-8205/794/1/l14. URL <http://dx.doi.org/10.1088/2041-8205/794/1/l14>.
- J. P. Hamaker, J. D. Bregman, and R. J. Sault. Understanding radio polarimetry. I. Mathematical foundations. *A&AS*, 117:137–147, May 1996.
- DC Hogg, FO Guiraud, and MT Decker. Measurement of excess radio transmission length on earth-space paths. *A&A*, 95:304–307, 1981.
- MA Holdaway. Calculation of anomalous refraction on chajnantor. 1997.

- MA Holdaway and DP Woody. Yet another look at anomalous refraction. 1998.
- T. Johannsen and D. Psaltis. Testing the No-hair Theorem with Observations in the Electromagnetic Spectrum. II. Black Hole Images. *ApJ*, 718:446–454, July 2010. doi: 10.1088/0004-637X/718/1/446.
- M. D. Johnson. Probing Strongly-Scattered Compact Objects Using Ultra-High-Resolution Techniques in Radio Astronomy. 2013.
- M. D. Johnson, V. L. Fish, S. S. Doeleman, A. E. Broderick, J. F. C. Wardle, and D. P. Marrone. Relative Astrometry of Compact Flaring Structures in Sgr A* with Polarimetric Very Long Baseline Interferometry. *ApJ*, 794:150, October 2014. doi: 10.1088/0004-637X/794/2/150.
- M. D. Johnson, V. L. Fish, S. S. Doeleman, D. P. Marrone, R. L. Plambeck, J. F. C. Wardle, K. Akiyama, K. Asada, C. Beaudoin, L. Blackburn, R. Blundell, G. C. Bower, C. Brinkerink, A. E. Broderick, R. Cappallo, A. A. Chael, G. B. Crew, J. Dexter, M. Dexter, R. Freund, P. Friberg, R. Gold, M. A. Gurwell, P. T. P. Ho, M. Honma, M. Inoue, M. Kosowsky, T. P. Krichbaum, J. Lamb, A. Loeb, R.-S. Lu, D. MacMahon, J. C. McKinney, J. M. Moran, R. Narayan, R. A. Primiani, D. Psaltis, A. E. E. Rogers, K. Rosenfeld, J. SooHoo, R. P. J. Tilanus, M. Titus, L. Vertatschitsch, J. Weintraub, M. Wright, K. H. Young, J. A. Zensus, and L. M. Ziurys. Resolved magnetic-field structure and variability near the event horizon of Sagittarius A. *Science*, 350(6265):1242–1245, dec 2015. doi: 10.1126/science.aac7087. URL <http://dx.doi.org/10.1126/science.aac7087>.
- M. D. Johnson, Y. Y. Kovalev, C. R. Gwinn, L. I. Gurvits, R. Narayan, J.-P. Macquart, D. L. Jauncey, P. A. Voitsik, J. M. Anderson, K. V. Sokolovsky, and M. M. Lisakov. Extreme Brightness Temperatures and Refractive Substructure in 3C273 with RadioAstron. *ApJ*, 820:L10, March 2016. doi: 10.3847/2041-8205/820/1/L10.

Michael D. Johnson and Carl R. Gwinn. THEORY AND SIMULATIONS OF REFRACTIVE SUBSTRUCTURE IN RESOLVED SCATTER-BROADENED IMAGES. *ApJ*, 805(2):180, jun 2015. doi: 10.1088/0004-637x/805/2/180. URL <http://dx.doi.org/10.1088/0004-637x/805/2/180>.

R Clark Jones. A new calculus for the treatment of optical systemsi. description and discussion of the calculus. *JOSA*, 31(7):488–493, 1941.

J. Kormendy and D. Richstone. Inward Bound—The Search For Supermassive Black Holes In Galactic Nuclei. *ARA&A*, 33:581, 1995. doi: 10.1146/annurev.aa.33.090195.003053.

M. Kramer, I. H. Stairs, R. N. Manchester, M. A. McLaughlin, A. G. Lyne, R. D. Ferdman, M. Burgay, D. R. Lorimer, A. Possenti, N. D’Amico, J. M. Sarkissian, G. B. Hobbs, J. E. Reynolds, P. C. C. Freire, and F. Camilo. Tests of General Relativity from Timing the Double Pulsar. *Science*, 314:97–102, October 2006. doi: 10.1126/science.1132305.

T. P. Krichbaum, D. A. Graham, A. Witzel, A. Greve, J. E. Wink, M. Grawing, F. Colomer, P. de Vicente, J. Gomez-Gonzalez, A. Baudry, and J. A. Zensus. VLBI observations of the galactic center source SGR A* at 86 GHz and 215 GHz. *A&A*, 335:L106–L110, July 1998.

James W Lamb and David Woody. Radiometric correction of anomalous refraction. *ALMA Millimeter Array Memo Series*, (224), 1998.

A. P. Lane. Submillimeter Transmission at South Pole. In G. Novak and R. Landsberg, editors, *Astrophysics From Antarctica*, volume 141 of *Astronomical Society of the Pacific Conference Series*, pages 289–295, 1998.

R G Lane, A Glindemann, and J C Dainty. Simulation of a Kolmogorov phase screen. *Waves in Random Media*, 2(3):209–224, jul 1992. doi: 10.1088/

- 0959-7174/2/3/003. URL <http://dx.doi.org/10.1088/0959-7174/2/3/003>.
- O. P. Lay. The temporal power spectrum of atmospheric fluctuations due to water vapor. *A&AS*, 122(3):535–545, may 1997. doi: 10.1051/aas:1997154. URL <http://dx.doi.org/10.1051/aas:1997154>.
- R.-S. Lu, T. P. Krichbaum, A. Eckart, S. König, D. Kunneriath, G. Witzel, A. Witzel, and J. A. Zensus. Multiwavelength VLBI observations of Sagittarius A*. *A&A*, 525:A76, January 2011. doi: 10.1051/0004-6361/200913807.
- R.-S. Lu, F. Roelofs, V. L. Fish, H. Shiokawa, S. S. Doeleman, C. F. Gammie, H. Falcke, T. P. Krichbaum, and J. A. Zensus. Imaging an Event Horizon: Mitigation of Source Variability of Sagittarius A*. *ApJ*, 817:173, February 2016. doi: 10.3847/0004-637X/817/2/173.
- Ru-Sen Lu, Avery E. Broderick, Fabien Baron, John D. Monnier, Vincent L. Fish, Sheperd S. Doeleman, and Victor Pankratius. IMAGING THE SUPERMASSIVE BLACK HOLE SHADOW AND JET BASE OF M87 WITH THE EVENT HORIZON TELESCOPE. *ApJ*, 788(2):120, may 2014. doi: 10.1088/0004-637x/788/2/120. URL <http://dx.doi.org/10.1088/0004-637x/788/2/120>.
- J.-P. Luminet. Image of a spherical black hole with thin accretion disk. *A&A*, 75:228–235, May 1979.
- J.-P. Macquart and G. C. Bower. Understanding the Radio Variability of Sagittarius A*. *ApJ*, 641:302–318, April 2006. doi: 10.1086/500317.
- J. Magorrian, S. Tremaine, D. Richstone, R. Bender, G. Bower, A. Dressler, S. M. Faber, K. Gebhardt, R. Green, C. Grillmair, J. Kormendy, and T. Lauer. The Demography of Massive Dark Objects in Galaxy Centers. *AJ*, 115:2285–2305, June 1998. doi: 10.1086/300353.

- D. P. Marrone, F. K. Baganoff, M. Morris, J. M. Moran, A. Ghez, S. Hornstein, D. Dowell, M. W. Bautz, G. R. Ricker, W. N. Brandt, G. P. Garmire, J. Lu, K. Matthews, G. Bower, J. Zhao, and R. Rao. An X-ray, IR, and Submillimeter Flare of Sagittarius A*. *38:112.06*, December 2006.
- D. P. Marrone, F. K. Baganoff, M. R. Morris, J. M. Moran, A. M. Ghez, S. D. Hornstein, C. D. Dowell, D. J. Muñoz, M. W. Bautz, G. R. Ricker, W. N. Brandt, G. P. Garmire, J. R. Lu, K. Matthews, J.-H. Zhao, R. Rao, and G. C. Bower. An X-Ray, Infrared, and Submillimeter Flare of Sagittarius A*. *ApJ*, 682:373–383, July 2008. doi: 10.1086/588806.
- C. R. Masson. Atmospheric Effects and Calibrations. In M. Ishiguro and J. Welch, editors, *IAU Colloq. 140: Astronomy with Millimeter and Submillimeter Wave Interferometry*, volume 59 of *Astronomical Society of the Pacific Conference Series*, pages 87–95, 1994.
- J. C. McKinney, A. Tchekhovskoy, A. Sadowski, and R. Narayan. Three-dimensional general relativistic radiation magnetohydrodynamical simulation of super-Eddington accretion, using a new code HARMRAD with M1 closure. *MNRAS*, 441:3177–3208, July 2014. doi: 10.1093/mnras/stu762.
- F. Melia. An accreting black hole model for Sagittarius A(*). 2: A detailed study. *ApJ*, 426:577–585, May 1994. doi: 10.1086/174094.
- A. Merloni, S. Heinz, and T. di Matteo. A Fundamental Plane of black hole activity. *MNRAS*, 345:1057–1076, November 2003. doi: 10.1046/j.1365-2966.2003.07017.x.
- L. Meyer, T. Do, A. Ghez, M. R. Morris, G. Witzel, A. Eckart, G. Bélanger, and R. Schödel. A 600 Minute Near-Infrared Light Curve of Sagittarius A*. *ApJ*, 688:L17, November 2008. doi: 10.1086/593147.
- M. Miyoshi, J. Moran, J. Herrnstein, L. Greenhill, N. Nakai, P. Diamond, and M. Inoue. Evidence for a black hole from high rotation velocities in a

- sub-parsec region of NGC4258. *Nature*, 373:127–129, January 1995. doi: 10.1038/373127a0.
- John D. Monnier. Phases in interferometry. *New Astronomy Reviews*, 51(8-9):604–616, oct 2007. doi: 10.1016/j.newar.2007.06.006. URL <http://dx.doi.org/10.1016/j.newar.2007.06.006>.
- M. Mościbrodzka, H. Falcke, H. Shiokawa, and C. F. Gammie. Observational appearance of inefficient accretion flows and jets in 3D GRMHD simulations: Application to Sagittarius A*. *A&A*, 570:A7, October 2014. doi: 10.1051/0004-6361/201424358.
- R. Narayan. The Physics of Pulsar Scintillation. *Philosophical Transactions of the Royal Society A: Mathematical Physical and Engineering Sciences*, 341(1660):151–165, oct 1992. doi: 10.1098/rsta.1992.0090. URL <http://dx.doi.org/10.1098/rsta.1992.0090>.
- R. Narayan and J. Goodman. The shape of a scatter-broadened image - I. Numerical simulations and physical principles. *MNRAS*, 238(3):963–994, jun 1989. doi: 10.1093/mnras/238.3.963. URL <http://dx.doi.org/10.1093/mnras/238.3.963>.
- R. Narayan and J. E. McClintock. Observational Evidence for Black Holes. *ArXiv e-prints*, December 2013.
- R. Narayan and I. Yi. Advection-dominated Accretion: Underfed Black Holes and Neutron Stars. *ApJ*, 452:710, October 1995. doi: 10.1086/176343.
- R. Narayan, I. V. Igumenshchev, and M. A. Abramowicz. Magnetically Arrested Disk: an Energetically Efficient Accretion Flow. *PASJ*, 55:L69–L72, December 2003. doi: 10.1093/pasj/55.6.L69.
- R. Narayan, J. E. McClintock, and A. Tchekhovskoy. Energy Extraction from Spinning Black Holes Via Relativistic Jets. page 523, 2014. doi: 10.1007/978-3-319-06349-2_25.

- Bojan Nikolic, Rosie C Bolton, Sarah F Graves, Richard E Hills, and John S Richer. Phase correction for ALMA with 183 GHz water vapour radiometers. *A&A*, 552:A104, 2013.
- J. E. Noordam and O. M. Smirnov. The MeqTrees software system and its use for third-generation calibration of radio interferometers. *A&A*, 524: A61, nov 2010. doi: 10.1051/0004-6361/201015013. URL <http://dx.doi.org/10.1051/0004-6361/201015013>.
- G. N. Ortiz-León, M. D. Johnson, S. S. Doeleman, L. Blackburn, V. L. Fish, L. Loinard, M. J. Reid, E. Castillo, A. A. Chael, A. Hernández-Gómez, D. H. Hughes, J. León-Tavares, R.-S. Lu, A. Montaña, G. Narayanan, K. Rosenfeld, D. Sánchez, F. P. Schloerb, Z.-q. Shen, H. Shiokawa, J. SooHoo, and L. Vertatschitsch. The Intrinsic Shape of Sagittarius A* at 3.5 mm Wavelength. *ApJ*, 824:40, June 2016. doi: 10.3847/0004-637X/824/1/40.
- J.R. Pardo, J. Cernicharo, and E. Serabyn. Atmospheric transmission at microwaves (ATM): an improved model for millimeter/submillimeter applications. *IEEE Trans. Antennas Propagat.*, 49(12):1683–1694, 2001. doi: 10.1109/8.982447. URL <http://dx.doi.org/10.1109/8.982447>.
- R. Penrose. Gravitational Collapse: the Role of General Relativity. *Nuovo Cimento Rivista Serie*, 1, 1969.
- A. Popping and R. Braun. The standing wave phenomenon in radio telescopes. *A&A*, 479(3):903–913, mar 2008. doi: 10.1051/0004-6361:20079122. URL <http://dx.doi.org/10.1051/0004-6361:20079122>.
- D. Psaltis, F. Özel, C.-K. Chan, and D. P. Marrone. A General Relativistic Null Hypothesis Test with Event Horizon Telescope Observations of the Black Hole Shadow in Sgr A*. *ApJ*, 814:115, December 2015. doi: 10.1088/0004-637X/814/2/115.

- Dimitrios Psaltis, Norbert Wex, and Michael Kramer. A QUANTITATIVE TEST OF THE NO-HAIR THEOREM WITH Sgr A* USING STARS PULSARS AND THE EVENT HORIZON TELESCOPE. *ApJ*, 818(2):121, feb 2016. doi: 10.3847/0004-637x/818/2/121. URL <http://dx.doi.org/10.3847/0004-637x/818/2/121>.
- S. J. Radford and M. A. Holdaway. Atmospheric conditions at a site for submillimeter-wavelength astronomy. In T. G. Phillips, editor, *Advanced Technology MMW, Radio, and Terahertz Telescopes*, volume 3357 of Proc. SPIE, pages 486–494, jul 1998.
- Alan E. E. Rogers, Sheperd S. Doeleman, and James M. Moran. Fringe detection methods for very long baseline arrays. *AJ*, 109:1391, mar 1995. doi: 10.1086/117371. URL <http://dx.doi.org/10.1086/117371>.
- E. Serabyn, J. Carlstrom, O. Lay, D. C. Lis, T. R. Hunter, J. H. Lacy, and R. E. Hills. High-Frequency Measurements of the Spectrum of Sagittarius A*. *ApJ*, 490(1):L77–L81, nov 1997. doi: 10.1086/311010. URL <http://dx.doi.org/10.1086/311010>.
- E. Serabyn, E. W. Weisstein, D. C. Lis, and J. R. Pardo. Submillimeter Fourier-transform spectrometer measurements of atmospheric opacity above Mauna Kea. *Appl. Opt.*, 37(12):2185, apr 1998. doi: 10.1364/ao.37.002185. URL <http://dx.doi.org/10.1364/ao.37.002185>.
- Z.-Q. Shen, K. Y. Lo, M.-C. Liang, P. T. P. Ho, and J.-H. Zhao. A size of \sim 1AU for the radio source Sgr A* at the centre of the Milky Way. *Nature*, 438:62–64, November 2005. doi: 10.1038/nature04205.
- J. Skilling and R. K. Bryan. Maximum Entropy Image Reconstruction - General Algorithm. *MNRAS*, 211:111, November 1984. doi: 10.1093/mnras/211.1.111.

- O. M. Smirnov. Revisiting the radio interferometer measurement equation. *A&A*, 527:A106, 2011a. doi: 10.1051/0004-6361/201016082. URL <http://dx.doi.org/10.1051/0004-6361/201016082>.
- O. M. Smirnov. Revisiting the radio interferometer measurement equation. *A&A*, 527:A107, 2011b. doi: 10.1051/0004-6361/201116434. URL <http://dx.doi.org/10.1051/0004-6361/201116434>.
- O. M. Smirnov. Revisiting the radio interferometer measurement equation. *A&A*, 527:A108, 2011c. doi: 10.1051/0004-6361/201116435. URL <http://dx.doi.org/10.1051/0004-6361/201116435>.
- O. M. Smirnov and C. Tasse. Radio interferometric gain calibration as a complex optimization problem. *MNRAS*, 449:2668–2684, May 2015. doi: 10.1093/mnras/stv418.
- O.M. Smirnov. presentation at ‘SKA CALIM workshop : Solving for primary beams, pointing errors, and The Westerbork Wobble’, Manchester, 25-29 July 2011., June 2011d. URL <https://indico.skatelescope.org/event/171/session/9/contribution/20>. (accessed June 13, 2016).
- R. Takahashi. Shapes and Positions of Black Hole Shadows in Accretion Disks and Spin Parameters of Black Holes. *ApJ*, 611:996–1004, August 2004. doi: 10.1086/422403.
- V. I. Tatarskii. The effects of the turbulent atmosphere on wave propagation. 1971.
- A. R. Thompson, J. M. Moran, and G. W. Swenson, Jr. *Interferometry and Synthesis in Radio Astronomy, 2nd Edition*. New York : John Wiley & Sons, 2001.
- R. N. Treuhhaft and G. E. Lanyi. The effect of the dynamic wet troposphere on radio interferometric measurements. *Radio Science*, 22(2):251–265, mar

1987. doi: 10.1029/rs022i002p00251. URL <http://dx.doi.org/10.1029/rs022i002p00251>.
- A. R. Whitney, I. I. Shapiro, A. E. E. Rogers, D. S. Robertson, C. A. Knight, T. A. Clark, R. M. Goldstein, G. E. Marandino, and N. R. Vandenberg. Quasars Revisited: Rapid Time Variations Observed Via Very-Long-Baseline Interferometry. *Science*, 173:225–230, July 1971. doi: 10.1126/science.173.3993.225.
- J. M. Wrobel and R. C. Walker. Sensitivity. 180:171, 1999.
- F. Yuan, E. Quataert, and R. Narayan. Nonthermal Electrons in Radiatively Inefficient Accretion Flow Models of Sagittarius A*. *ApJ*, 598:301–312, November 2003. doi: 10.1086/378716.
- F. Yusef-Zadeh, D. Roberts, M. Wardle, C. O. Heinke, and G. C. Bower. Flaring Activity of Sagittarius A* at 43 and 22 GHz: Evidence for Expanding Hot Plasma. *ApJ*, 650:189–194, October 2006. doi: 10.1086/506375.